Title

Dopamine Dynamics Underlying Alloparental Behavioral Acquisition Facilitated by Top-down Orbitofrontal Inputs in Female Mice

Short Title

Orbitofrontal Cortex for Maternal Behavior in Mice

Authors

Gen-ichi Tasaka[1,2*], Mitsue Hagihara[1], Satsuki Irie[1], Haruna Kobayashi[1], Kengo Inada[1], Kenta Kobayashi[3], Shigeki Kato[4], Kazuto Kobayashi[4], and Kazunari Miyamichi[1,5*]

Affiliations

[1] Laboratory for Comparative Connectomics, RIKEN Center for Biosystems Dynamics Research, Kobe, Hyogo 650-0047, Japan

[2] Japan Science and Technology Agency, PRESTO, Kawaguchi, Saitama 332-0012, Japan

[3] Section of Viral Vector Development, National Institute for Physiological Sciences, Okazaki, 444-8585, Japan.

[4] Department of Molecular Genetics, Institute of Biomedical Sciences, Fukushima Medical University School of Medicine, Fukushima 960-1295, Japan.

[5] Lead contact

*Corresponding author: genichi.tasaka@riken.jp; kazunari.miyamichi@riken.jp

Abstract

Maternal behaviors, which are crucial for the survival of mammalian infants, require the coordinated operation of multiple brain regions to process infant cues, make decisions, and execute motor plans. Although these processes likely demand higher cognitive functions, the top-down regulation of limbic parental programs remains poorly understood. Here, we show that the orbitofrontal cortex (OFC) excitatory projection neurons promote alloparental caregiving behaviors in female mice. By chronic microendoscopy, we observed robust yet adaptable representations of pup-directed anticipatory and motor-related activities within the OFC that significantly overlapped with those related to nonsocial reward signals. The inactivation of OFC output reduced the phasic activities of midbrain dopamine (DA) neurons specifically tied to pup retrieval and impaired the modulation of DA release to the ventral striatum during the acquisition of alloparental behaviors. Collectively, our study identifies top-down signals from the OFC that modulate the plasticity of the DA system, thereby promoting alloparental behaviors.

Teaser

Orbitofrontal cortex neurons facilitate alloparental behaviors in virgin female mice by modulating

the dopamine system.

MAIN TEXT

Introduction

Maternal behaviors, including feeding and protection of the young, are crucial for the physical and mental health of mammalian infants (*1*). To achieve these behaviors, many brain areas must work together to process infant cues, make decisions, and generate motor planning and execution, which likely requires higher cognitive function of the brain. Although classical models of neural circuits for parental behaviors often assume the prefrontal cortex (PFC) as an integrator of infant-related sensory signals and a controller of decision-making and motivation (*1, 2*), these ideas are mostly based on anatomical studies and have not been functionally tested. On one hand, maternal behaviors are triggered by a pup's sensory signals, and a large body of research has examined maternal plasticity in sensory coding in the olfactory and auditory regions (*3-8*). On the other hand, classical lesion and pharmacological manipulation studies in rats have emphasized the importance of the medial preoptic area and its downstream mesolimbic dopamine (DA) system in maternal caregiving motivation (*9*). Recent molecular genetic studies in mice have described more precise circuit architectures of subcortical parental behavioral centers at the resolution of specific cell types (*10-14*). In contrast to these advances in understanding cortical sensory systems and subcortical parental behavioral centers, the functional organization of the PFC that potentially links sensory signals to maternal behavioral execution remains mostly elusive (*15*). As such, little is known about how subcortical regions are regulated by the cortical top-down inputs in the context of maternal behaviors.

There is accumulating evidence that the PFC is involved in many aspects of social behaviors, such as social dominance (*16, 17*), sexual behaviors (*18*), and social observational fear learning (*19, 20*). Although most previous studies have focused on the medial PFC (mPFC), a recent study reported that the orbitofrontal cortex (OFC) of mother mice is activated by the ultrasonic vocalizations of pups (*4*). Imaging studies in humans have also shown that visual and auditory signals related to children evoke activity in the OFC of mothers (*21, 22*). The OFC is generally thought to facilitate the transition between sensation and action by associating diverse sensory signals with valence in behavioral contexts (*23-26*). Furthermore, recent studies have revealed that individual OFC neurons encode diverse representations of behaviorally relevant features, including sensory signals, spatial locations, and cues that predict reward outcomes, as well as rewards *per se* (*27-29*). However, the neural representations or functions of the OFC in guiding naturally occurring behaviors, such as maternal caregiving behaviors, remain unexplored. This knowledge gap motivated us to explore the functional representations of pup-directed caregiving behaviors in the OFC of female mice.

Mothers are innately motivated to care for their young with strong rewards (*30*). The ventral tegmental area (VTA) in the midbrain, where most DA neurons are located, is one of the most well-characterized regions for reinforcement learning (*31, 32*). The neural activity of DA neurons in the VTA (VTA^{DA} neurons) ramps up during pup retrieval (*11*), a hallmark of maternal caregiving behaviors, and gradually decreases as female mice experience more pup retrieval (*33*). This

dynamics of VTA^{DA} neuron activity is thought to reflect reward prediction error (RPE) to guide reinforcement learning (*33*), although the precise neural mechanisms underlying such plasticity remain largely unknown. Pharmacological or optogenetic inactivation of VTA^{DA} neurons disrupts pup retrieval (*33, 34*), underscoring their crucial role in maternal motivation toward infants. Notably, the OFC projects to the VTA, potentially contributing to reward-based learning (*35-37*). Therefore, we hypothesize that the OFC provides top-down efferents conveying pup-related information to the VTA^{DA} neurons, which may underlie the motivation for maternal behaviors.

Virgin female mice can exhibit maternal caregiving behaviors, such as pup retrieval, following instruction, observation of experienced caretakers (*38, 39*), or repeated exposure to infants (*40*). We chose to focus on the emergence of maternal retrieval behaviors in virgin female mice (alloparental pup retrieval) for two reasons. First, unlike the rapid onset of maternal behaviors in biological mothers, alloparental retrieval develops gradually and slowly in virgin females (*33, 39*), allowing us to characterize the varying neural correlates of increasing behavioral performance and the dynamics of neural activities during these processes. Second, once maternal behaviors are established, they are robust (*41*). The alloparental paradigm may be particularly suited for characterizing the potentially nuanced modulatory roles of the higher cognitive areas in maternal behaviors. Therefore, we employed a combination of viral-genetic manipulation and chronic microendoscopic calcium (Ca^{2+}) imaging to examine the functions of the OFC in the acquisition of alloparental pup retrieval behaviors in virgin female mice.

Results

OFC layer 5 neurons are required for the efficient acquisition of alloparental pup retrieval

The OFC is characterized by a thick layer 5 that projects to various subcortical regions (*42*). By employing the *Rbp4-Cre* line (*43*), an excitatory layer 5-specific Cre driver, we focused on the excitatory layer 5 pyramidal cells in the OFC (OFC^{Rbp4} neurons). To examine the role of OFC^{Rbp4} neurons in alloparental behaviors, we utilized active caspase-mediated genetic cell ablation (*44*). We injected an adeno-associated virus (AAV) encoding taCasp3-TEVp in *Rbp4-Cre* mice crossed with the *Ai162* reporter line as a marker, which expresses GCaMP6s in a Cre-dependent manner (*45*) (Fig. 1A). The injection of AAV encoding taCasp3 significantly reduced the number of GCaMP6s-expressing (+) cells by approximately 30%, as compared to the phosphate-buffered saline (PBS)-injected side (Fig. 1B–C). To assess the effects of this mild ablation of OFC^{Rbp4} neurons, we employed the alloparental training paradigm (*39*), cohousing virgin female mice with a mother and pups. The retrieval success rates, defined as the fraction of females showing retrieval of all six pups within 4 min, were measured before and at 1 or 2 days after cohousing (Fig. 1D) (*3, 39*). The latency to investigate the pups did not show statistical differences, suggesting similar levels of attention toward pups in both groups (Fig. 1E). Prior to cohousing, the vast majority of virgin females did not show spontaneous pup retrieval. After 2 days of cohousing, virgin females in the control group achieved a 100% retrieval success with a shortened latency (Fig. 1F). Of note, this relatively rapid

behavioral acquisition, compared to previous studies (*39*), may be attributed to the genetic background of our study, which utilized an F1 hybrid of B57BL/6J and FVB strains. By contrast, half of the OFC^{Rbp4}-ablated group did not achieve successful retrieval, demonstrating a significant impairment in the acquisition of alloparental pup retrieval, accompanied by a significantly longer latency to complete the retrieval (Fig. 1G, H).

To investigate whether the activity of OFC^{Rbp4} neurons during pup exposure contributes to the induction of pup retrieval, we employed an inhibitory optogenetic approach coupled with repetitive pup exposure to induce alloparental pup retrieval in virgin female mice (*40*). We administered AAVs encoding the inhibitory opsin GtACR2, with mCherry serving as a control, into the OFC of *Rbp4-Cre* mice (Fig. 1I–K). Subsequently, optic fibers were bilaterally implanted above the OFC for optogenetic manipulation. The virgins were exposed to three pups in a small home cage for 15 min per day, followed by a 4-min pup retrieval assay. Throughout both the exposure and retrieval sessions, the OFC^{Rbp4} neurons were silenced (Fig. 1K). Before pup exposure, these female mice did not exhibit spontaneous pup retrieval, regardless of the manipulation (Fig. 1L–M). Although the latency to investigate the pups remained constant, the optogenetic silencing of OFC^{Rbp4} neurons resulted in a reduction in successful retrievals by virgin females, accompanied by a significantly longer latency to complete the retrieval (Fig. 1L–O). These data suggest that the acute involvement of OFC^{Rbp4} neurons is required to facilitate alloparental pup retrieval during short-term desensitization to pups.

Temporal dynamics of pup retrieval-related responses in OFC^{Rbp4} neurons

OFC^{Rbp4} neurons contribute to alloparental pup retrieval, and thus, we next investigate a neural representation of such behaviors within these neurons. To this end, we utilized microendoscopic Ca^{2+} imaging (*46*) in *Rbp4-Cre*; *Ai162* female mice, which were surgically implanted with a gradient refractive index (GRIN) lens (500-μm diameter) above layer 5 of the OFC. The expression of GCaMP6s and the placement of the lens were histologically confirmed (Fig. S1A). Fig. 2A–E illustrates a representative example of cohousing day 2 virgin females during the pup retrieval assay, with 60 regions of interest (ROIs; putatively corresponding to individual cells) within the field of view. Pup retrieval involves three major behavioral categories (in the following sequence): interaction with a pup, retrieval onset, and placing a pup into the nest (completion) (Fig. 2C). We defined physical contact between a female and a pup as interaction, which typically lasted 1.1 seconds before transitioning to pup retrieval. The average duration of pup retrieval was 2.0 seconds. We observed that certain ROIs exhibited an increased Ca^{2+} transient (referred to as an elevated response) synchronized with these three behavioral categories (Fig. 2D, E). Moreover, some ROIs displayed elevated responses just before the interaction (as indicated by the gray traces in Fig. 2E). We term this category as anticipatory, suggesting the presence of a subpopulation of OFC^{Rbp4} neurons encoding premotor or sensory-related signals. In addition to these elevated responses, we identified distinct ROIs showing a significantly decreased (suppressed) response during the

anticipatory, interaction, onset, or completion of pup retrieval (Fig. 2F). These responsive ROIs were dispersed throughout the field of view without forming noticeable spatial clusters (Fig. 2G).

To monitor potential modulations in OFC^{Rbp4} neuron responses during pup retrieval across the behavioral acquisition process, we conducted chronic imaging on the same animals at various stages: before cohousing, 1 or 2 days after cohousing, and after the transition to biological motherhood (Fig. 3A). At each stage, we conducted two consecutive 6-min recording sessions in which new pups were promptly presented upon the retrieval of existing ones. To compare OFC^{Rbp4} neuron activity patterns among virgin females with different levels of retrieval performance, we designated the first day on which virgin females retrieved five or more pups within a session as alloparental day 1 (AP1). During AP1, the total number of pup retrievals was small, and the fraction of interactions with pups followed by retrieval was low (Fig. S1B, C). By contrast, on the subsequent day of cohousing (AP2), these parameters significantly increased, and virgin females exhibited pup retrieval proficiency comparable to lactating mothers (Mother; corresponding to 2–4 postpartum days) (Fig. S1C).

To visualize the temporal dynamics of Ca^{2+} responses, ROIs were sorted based on the time of their maximum responses aligned with the onset of pup interaction to construct activity heat maps (Fig. 3B). Across AP1, AP2, and Mother, the peak response times tiled the entire pup retrieval sequence, including anticipatory periods, illustrating that OFC^{Rbp4} neurons collectively cover all sequential actions. As each ROI exhibited either elevated or suppressed responses during specific pup retrieval time windows without displaying bimodal patterns (Fig. 3B), we classified responsive ROIs into eight subgroups based on the nature of their responses (elevated or suppressed) and the behavioral categories to which the Ca^{2+} transients were temporally linked (anticipatory, interaction, retrieval onset, and completion) (Fig. 3C, D). Ca^{2+} responses locked with behaviors were consistently detected across AP1, AP2, and Mother, with the fraction of elevated-responsive ROIs decreasing significantly with increases in performance levels (Fig. 3C). Half of the elevated-responsive ROIs were time-locked to the onset of retrieval, while the largest fraction of suppressed reactions was locked to the interaction (Fig. 3D), a trend observed across AP1, AP2, and Mother.

To compare the responses to each behavior between groups, population-weighted responses were calculated by multiplying the averaged response by the responsive fraction. Elevated responses during interaction and completion significantly decreased between AP1 and AP2, whereas suppressed responses during the anticipatory stage significantly increased in AP2 (Fig. 3E, F). These changes seem to reflect alterations in the responsive fraction (Fig. 3D), as the response amplitude remained largely unchanged (Fig. S1D, E). These data suggest that the overall population responses in OFC^{Rbp4} neurons are suppressed in AP2 due to decreased elevated responses and increased suppressed responses.

To explore whether OFC^{Rbp4} neurons elicit responses during pup retrieval even in the absence of preceding interactions with pups, we artificially induced pup retrieval in virgin females by

activating oxytocin (OT) neurons in the paraventricular hypothalamic nucleus (PVH) (Fig. S2A, B) (*8*). An AAV carrying *hM3D(Gq)-Myc* under an *OT* promoter (*47*) was introduced into the PVH. The expression of Gq-Myc was confirmed through immunostaining (Fig. S2C). Administration of clozapine-N-oxide (CNO) significantly facilitated pup retrieval (Fig. S2D). We observed that OT neuron-activated virgins demonstrated neural responses to all behavioral categories of pup retrieval (Fig. S2E–I), closely resembling those observed in cohoused females (Figs. 2 and 3). These data align with the view that OFC^{Rbp4} neurons can promptly be tuned to respond during pup retrieval, even without prior cohousing or sensitization.

Decoding capability of OFC^{Rbp4} neurons

We next sought to investigate the decoding capability of OFC^{Rbp4} neurons among AP1, AP2, and Mother. We trained a linear support vector machine (SVM) to classify different behavioral categories of pup retrieval (Methods). Classification accuracies showed an increase with more ROIs being used to train the SVM. Notably, the accuracies remained comparable between AP1 and AP2, despite the overall decrease in elevated responders in AP2, and were also similar between virgin females and Mother (Fig. 3G). Shuffling the data or excluding significantly responsive ROIs (color-categorized ones in the heat map) markedly decreased classification accuracy, approaching chance levels (Fig. 3G, H). This suggests that significantly responsive cells in the OFC carry adequate information to decode behavioral categories during pup retrieval.

Considering that not all interaction trials were followed by pup retrieval (Fig. S1C), we also analyzed the activities of OFC^{Rbp4} neurons during non-retrieval trials. Activity heat maps revealed that both elevated and suppressed responses to all behavioral categories were weak during the non-retrieval trials (Fig. S3A). Overall, the intensities of both elevated and suppressed responses during anticipatory and interaction periods were significantly diminished in non-retrieval trials (Fig. S3B–E), although a small fraction of ROIs exhibited a weak but significant response (Fig. S3F, G). Thus, most responses during pup retrieval are behavior-locked, and weak responses in the anticipatory and interaction categories may be attributed to pup-related sensory stimuli.

Subsequently, we assessed whether the SVM could predict whether a trial would result in retrieval or not based on OFC activity during interaction. We found that the OFC population activities of AP1, AP2, and Mother were all sufficient to predict whether the trial involved retrieval (Fig. 3I). These results suggest that the coding capability of pup retrieval within OFC^{Rbp4} neurons is maintained across AP1, AP2, and Mother. Considering the overall reduction in elevated responses in AP2 and Mother (Fig. 3E), fine-tuning of behavioral coding might occur as the performance levels increase.

Substantial overlap between OFC^{Rbp4} neurons responsive to pup retrieval and reward

Mothers are innately motivated to care for their pups with strong rewards (*30*). Therefore, we hypothesized that retrieval-responsive neurons encode some degree of positive valence. To test this,

we examined the extent of overlap between OFC^{Rbp4} neurons responding to pup retrieval and those activated by nonsocial rewards. We used sugar water (10% sucrose) as a nonsocial reward for water-deprived mice (Fig. 4A). To identify the responses to pup retrieval and the sugar water reward within the same ROIs, we conducted Ca^{2+} imaging for pup retrieval and water licking in the same imaging sessions with freely moving animals (Fig. 4B–C). We identified 98 and 30 ROIs displaying elevated responses to pup retrieval and the nonsocial reward, respectively, suggesting that OFC^{Rbp4} neurons responsive to pup retrieval outnumber those responding to nonsocial cues (Fig. 4D, E). Notably, 47% of water-reward-responding ROIs were also active during pup retrieval. Regarding suppressed responses, we identified 184 and 133 ROIs responding to pup retrieval and the nonsocial reward, respectively, with substantial overlap between them (Fig. 4D, E). These overlaps were significantly greater than chance (Fig. 4F). Taken together, under the constraints of the behavioral paradigm (see Discussion), these observations align with the view that representations of pup retrieval in OFC^{Rbp4} neurons are related to a reward.

OFC facilitates pup retrieval-related activities of DA neurons across multiple temporal scales

Our study thus far has revealed that OFC^{Rbp4} neurons exhibit a neural representation of pup retrieval and are required for the efficient acquisition of maternal behaviors. How do OFC^{Rbp4} neurons facilitate behavioral acquisition in the downstream neural circuit? Given that VTA^{DA} neurons can be directly regulated by OFC (*36*) and critically guide maternal motivation toward infants (*33*), we next aimed to characterize VTA^{DA} neurons as a potential output of the OFC. We first confirmed the direct projections from OFC^{Rbp4} neurons to the VTA (Fig. S4). Subsequently, we employed optogenetic silencing of the OFC in combination with Ca^{2+} imaging of VTA^{DA} neurons using fiber photometry (Fig. 5A). We injected AAVs encoding the inhibitory opsin GtACR2, with YFP as a control, into the OFC of *DAT-Cre* mice (*48*) crossed with *Ai162* mice (Fig. 5B, C). Two weeks later, we bilaterally implanted optic fibers just above the OFC for optogenetic manipulation and another one into the left VTA for fiber photometry. We validated that GCaMP6s was selectively expressed by DA neurons in the *DAT-Cre*; *Ai162* mice using fluorescent *in situ* hybridization (Fig. 5D).

We conducted four sessions of pup retrieval assays, each lasting 2.5 min, while simultaneously performing imaging, with and without laser stimulation (Fig. 5B). Throughout each session, new pups were presented immediately upon the retrieval of existing ones. The total number of retrieved pups increased as animals progressed from AP1 to Mother. However, we observed that acute silencing of the OFC resulted in a reduction in the number of retrievals in the AP1 group, whereas the number of retrievals in AP2 and Mother remained unchanged (Fig. 5E). These behavioral data align with the loss-of-function experiments (Fig. 1), supporting the role of the OFC in the early phase of behavioral acquisition.

To assess the influence of silencing OFC neurons on VTA^{DA} neuron activity, we compared the Ca^{2+} transients of VTA^{DA} neurons with and without laser stimulation around the peri-events of pup retrievals. Consistent with previous reports (*11, 33*), VTA^{DA} neurons exhibited time-locked

activity following pup interaction (Fig. 5F). Non-retrieval trials did not show a significant photometry signal of VTA^{DA} neurons, indicating that the phasic activity of these neurons during pup retrieval is behaviorally relevant. Silencing the OFC led to a significant decrease in the Ca^{2+} activity of VTA^{DA} neurons in the AP1 and AP2 groups (Fig. 5G, H). The reduction in VTA^{DA} neuron activity was more pronounced in AP1 than in AP2, while no such effect was observed in the Mother group. Taken together, these data show that the OFC facilitates VTA^{DA} neuron activity during pup retrieval, particularly in the early stages of maternal behavioral acquisition.

Consistent with recent research proposing that VTA^{DA} neurons encode RPE during retrieval learning (*33*), we also observed a significant overall decline in retrieval-related activities of VTA^{DA} neurons as animals progressed from AP1 to Mother, with the response magnitude inversely correlated with the performance (Fig. 5I, top). By contrast, silencing of the OFC attenuated this reduction (Fig. 5I), suggesting that the OFC is involved in the experience-dependent plasticity of VTA^{DA} neuron activity.

We next investigated the potential role of the OFC in modulating the temporal dynamics of VTA^{DA} neurons in a trial-by-trial manner. In the absence of OFC inactivation, we observed a more intensive response during the first five as compared to the last five retrieval trials, as inferred by the peak height of the photometric signals, across AP1, AP2, and Mother (Fig. 6A). By contrast, the silencing the OFC canceled the differences between the first and last five trials in AP1 and AP2, while the OFC no longer affected the dynamics of VTA^{DA} neuron activity within the session in the Mother group. These data indicate that i) VTA^{DA} neuron activity rapidly adapts during individual sessions, even within a single day, a phenomenon we term the "adaptation", and ii) the OFC is involved in encoding the adaptation in virgin females, while its influence on the adaptation disappears during the biological transition to motherhood.

We also noted that, in the absence of OFC inactivation, significantly larger VTA^{DA} neuron signals were observed in retrieval trials following a non-retrieving trial, compared with those subsequent to a successful retrieval (Fig. 6B, left); we term this phenomenon the "history dependency." The silencing of the OFC disrupted this history dependency (Fig. 6B, right). Additionally, we found that the activity levels of VTA^{DA} neurons during the retrieval trials were comparable, irrespective of the success or failure of the following trials, suggesting that no variation in VTA^{DA} neuron activity influences the behavioral outcome in subsequent trials (Fig. S4C). Collectively, these data highlight the OFC-mediated dynamic modulation of VTA^{DA} neuron activity across various temporal scales (Fig. 6C).

OFC facilitates DA release into the ventral striatum (VS)

VTA^{DA} neurons send their axons to various downstream regions, including different subregions of the striatum and amygdala (*49*). Although a recent study utilizing a genetically encoded fluorescent DA sensor (*50*) demonstrated DA release into the VS during pup retrieval (*51*), the regional diversity of DA signaling during pup retrieval remains unexplored. To address this issue, we virally targeted

GRAB^{DA3m} to the following four specific regions for photometric recording: the VS, dorsal striatum (DS), posterior striatum (PS), and basolateral amygdala (BLA) (Fig. 7A, B). Representative traces of regional DA signals are shown in Fig. 7C. We observed significant DA transients during pup retrieval compared with the non-retrieval trials across all regions, suggesting their potential contribution to pup retrieval behaviors (Fig. 7D). Specifically, area under the receiver operating characteristic curve (AUC-ROC) analysis showed that the DA transients reached statistical significance just before or after the interaction with a pup across all the regions (Fig. 7E). To assess the regional diversity of DA signaling, we compared the phasic DA traces among the different regions (Fig. 7F). We observed the largest DA transients during the pup retrieval trials in the VS (Fig. 7F), with the BLA exhibiting a longer latency to peak than the other regions. Furthermore, the VS exhibited a larger full-width-half-maximum (FWHM) than the DS and PS, indicating the region-specific temporal dynamics of DA transients. These findings highlight the heterogeneous nature of DA signaling and its temporal regulation across targeted subregions during pup retrieval.

Lastly, we investigated the role of the OFC in DA release in the VS, given the most pronounced DA transient observed, along with previous research suggesting the importance of the VTA–VS circuit in maternal behaviors (*52, 53*). Due to spatial constraints, optogenetic manipulation in the OFC influenced GRAB^{DA3m} signals in the VS. Hence, we utilized a chemogenetic approach. An AAV expressing Cre-dependent hM4Di(Gi)-mCherry was injected into the bilateral OFC of *Rbp4-Cre* animals, along with another AAV expressing GRAB^{DA3m} into the VS (Fig. 8A). We monitored the GRAB^{DA3m} signal during pup retrieval while the OFC^{Rbp4} neurons were silenced by CNO administration (Fig. 8B). Post hoc histological analyses confirmed the precision of targeting for hM4Di-mCherry and the GRAB sensor (Fig. 8C, D). While CNO administration in mCherry-expressing control animals showed no impact on DA release during pup retrieval, chemogenetic silencing of OFC^{Rbp4} neurons resulted in a significant reduction in DA release in the VS in AP1, but not in AP2 or Mother (Fig. 8E). These data align with the findings that OFC silencing has a more pronounced impact on VTA^{DA} neuron activity in AP1 (Fig. 5H). Collectively, these data demonstrate that the OFC facilitates DA release into the VS during pup retrieval, particularly in the early stages of maternal behavioral acquisition, potentially contributing to the efficient acquisition of maternal behaviors.

Discussion

During the last decade, there has been intensive research on the limbic circuits for parental behaviors (*10, 54*). However, our understanding of the potential functions of PFC in parental behaviors remains limited. Given the substantial evolutionary expansion of the human frontal cortex, understanding the higher-order functions associated with parental behaviors and the potential interactions between the frontal cortex and limbic circuits during such behaviors could be expected to offer valuable insights into human parental behaviors. The present study characterizes the functions of top-down circuits

originating from the OFC that modulate the plasticity of the DA system (Fig. S5). Here, we discuss the insights obtained from our study and its limitations.

Roles of the OFC in maternal behaviors

In contrast to the parental behavior centers in the preoptic area, such as galanin neurons (*1, 10*) or Calcr neurons (*13*), whose dysfunction completely blocks maternal caregiving, our data suggest that the OFC has a modulatory role on the acquisition of parental behaviors. Both cell ablation and optogenetic inhibition of the OFC delayed the acquisition of maternal behaviors following cohousing with mothers and pups or repeated exposures to pups (Fig. 1), implying the involvement of the OFC in linking pups with innate values. Supporting this notion, OFC^{Rbp4} neurons responsive to pup retrieval also exhibited a significant overlap in response to nonsocial rewards (Fig. 4). Moreover, the OFC played a role in modulating DA neuron activity (Figs. 5 and 6) and DA release in the VS (Fig. 8), a core component of the brain's reward system. Collectively, the OFC may enhance motivation to drive maternal behaviors during the process of behavioral acquisition, conceptualizing pups as rewards (Fig. S5).

While decades of research utilizing sophisticated learning paradigms have shown the role of the OFC in value-based decision-making and reversal learning by representing and updating subjective values (*23, 55, 56*), relatively little attention has been paid to the neural representations of the OFC during naturally occurring behavioral acquisition. Our data offer several insights. First, the OFC harbors a largely stable representation of pup retrieval (Fig. 3), which can emerge even without prior experience of pup retrieval (Fig. S2). This may reflect the intrinsic value of instinctive behaviors and contrasts with the prevailing view that the PFC can modulate social behaviors based on its flexible coding shaped by prior experiences or learning (*57-59*). Second, within these overall stable representations, there is a noticeable change in the cells responsive to pup interaction, such as a significant reduction in population activity over experience (Fig. 3). This reduction mirrors the decline in activity over experience observed in the downstream VTA^{DA} neurons (Figs. 5 and 6). While we interpret these declines as a fine-tuning process, determining their precise roles in pup retrieval requires future studies.

We recognize several limitations in the present study. First, despite our focus on the OFC due to its neural activation by infant-related sensory inputs in both humans and mice (*4, 21, 22*), we did not examine the regional specificity of the OFC in regulating maternal behavioral acquisition. Other areas of the frontal cortex, such as the mPFC (*15*) and the anterior cingulate cortex (*60*), may have significant roles alongside the OFC. Second, although we found OFC^{Rbp4} neurons whose activities tiled all behavioral categories of pup retrieval, it remains unclear whether these distinct populations are associated with subtypes of neurons based on their axonal projection or gene expression profiles (*42, 61*). As projection-defined neurons can encode unique or overlapping information (*36, 62*), future studies should address whether transcriptional types or projection-defined neurons in the OFC convey unique information about pup retrieval to specific downstream targets. Third, we

acknowledge that variations in internal states may complicate comparisons of the responsiveness of OFC^{Rbp4} during pup retrieval to nonsocial rewards (Fig. 4). For instance, the reward magnitude depends on the internal state, as sugar water does not serve as a reward for a satiated animal (*63*). Future studies should develop imaging or recording protocols capable of analyzing multiple task categories where reward scales can be controlled.

Roles of the DA system in maternal behaviors

While previous studies have established roles of VTA^{DA} neurons in maternal behaviors (*34*), the mechanisms underlying the temporal dynamics of their neural activity during pup retrieval (*11, 33*) have remained elusive. Our data demonstrate a functional link through which OFC neurons facilitate pup-retrieval-locked VTA^{DA} neuron activities only during the early stages of behavioral acquisition (Fig. 5). As behavioral performance improves, the OFC-mediated enhancement of VTA^{DA} activity gradually disappears, which accounts for the experience-dependent gradual decline in VTA^{DA} activity (*33*) (Figs. 5 and 6). Specifically, we identified two components underlying the regulation of VTA^{DA} activity dynamics by the OFC: adaptation and history dependency. Analogous to the known representation of behavioral novelty and saliency in VTA^{DA} neurons (*64*), these factors may play roles in learning, reinforcement, and motivation. In sensory systems, neural adaptation to repetitive stimuli often enhances sensitivity to unexpected stimuli (*65*). Thus, one possibility is that VTA^{DA} neuron adaptation enhances the detectability of novel or unexpected behavioral outcomes. The derivative of the DA signal is crucial for reinforcement learning, as VTA^{DA} transients facilitate the association of behavioral outcomes with preceding events (*66*). The history dependency observed in this study may function in updating state representations to facilitate the association of behavioral outcomes with preceding events or cues.

A recent study proposed a social RPE model (*33*), suggesting that the experience-dependent reduction in VTA^{DA} neuron activity is attributed to pup-related cues preceding the interaction. Given that the inactivation of the OFC abolished this RPE-like decline in VTA^{DA} neuron activity, one intriguing possibility is that OFC activities, particularly those time-locked to anticipatory and interaction categories, contribute to generating social RPE signals. While the concept of RPE signals is instrumental in enabling animals to update internal representations of their environment and adapt their behavior, the biological implementation of RPE in maternal behaviors remains largely unknown. Therefore, it is important to investigate how the OFC loses its influence on VTA^{DA} activities during the biological transition to motherhood. Maternal plasticity in the neural circuits between the OFC and VTA^{DA} neurons, particularly the direct axonal projections from the OFC to VTA^{DA} neurons, presents an interesting target (*35, 36*), although multiple synaptic pathways (*67*) involving GABAergic or glutamatergic neurons may also be significant. Additionally, understanding how VTA^{DA} neuron activity is modulated in mothers after the loss of OFC involvement is important. One critical region in this context is the medial preoptic area, where estrogen receptor alpha-expressing cells facilitate VTA^{DA} neuron activity during pup retrieval by inhibiting non-DA neurons in the VTA

(*11*). Future investigations should elucidate the precise circuit mechanisms underlying VTA^{DA} neural dynamics and their plasticity during the acquisition and maintenance of maternal behaviors.

Subtypes of DA neurons, based on their molecular profiles and anatomical positions, project their axons toward partially overlapping yet distinct downstream targets (*36, 68*). This organization contributes to variations in DA release, which may not directly correlate with overall somatic neural activity (*69, 70*). Recent rodent studies have elucidated the functional heterogeneity among VTA^{DA} neurons across various targeted regions. For instance, DA release in the VS is linked to reward, motivation, and learning, whereas in the DS, it regulates motor function (*69, 70*). DA release in the tail of the striatum is associated with processing aversive stimuli (*71*), and in the BLA, it modulates emotional processing and fear conditioning (*72*). Despite these advancements, the dynamics of DA release during maternal behaviors have only been characterized in the VS (*51*). Our data not only support pronounced DA release in the VS during pup retrieval, but also demonstrate the presence of reliable phasic DA transients with various temporal dynamics observed across all regions, including the DS, PS, and BLA. Consequently, we expect that future research will focus on recording VTA^{DA} neurons at single-cell resolution and manipulating their specific projection types to elucidate the heterogeneous roles played by distinct subtypes of VTA^{DA} neurons in the regulation of maternal behaviors.

Acknowledgments

We thank Liqun Luo, Adi Mizrahi, Ido Maor, and members of the Miyamichi lab for the critical reading of the manuscript, the University of North Carolina vector core and the Canadian Neurophotonics Platform viral vector core facility for the AAV productions, Masanori Murayama for sharing the *Rbp4-Cre* mice, Noriaki Ohkawa for the advice on the miniaturized microscope, Kentaro Ishii for the advice on the decoder analysis, and the animal facility of RIKEN BDR for taking care of the animals and *in vitro* fertilization. This work was supported by the JST PRESTO program (JPMJPR21S7), JSPS KAKENHI (20K15941), and RIKEN incentive and diversity promotion grants to G.T., the Brain/MINDS program from AMED (JP21dm0207113) to Ka.K, and a Takeda Science Foundation Research Grant, JSPS KAKENHI (20K20589, 21H02587), and a RIKEN BDR Stage-Transition Project grant to K.M.

Author Contributions

G.T. and K.M. conceived the experiments. G.T. performed all the experiments and analyzed the data, with technical support from M.H., S.I., and H.K. K.I. and M.H. provided the AAV *OTp-hM3D(Gq)-Myc*, Ke.K. generated AAVrg *CAG-FLEx-FlpO*, and S.K. and Ka.K. generated AAVdj *hSyn-DIO-hM4Di-mCherry*. G.T. and K.M. wrote the paper with help from all authors.

Declaration of Interests

The authors declare that they have no competing interests.

Main Figures

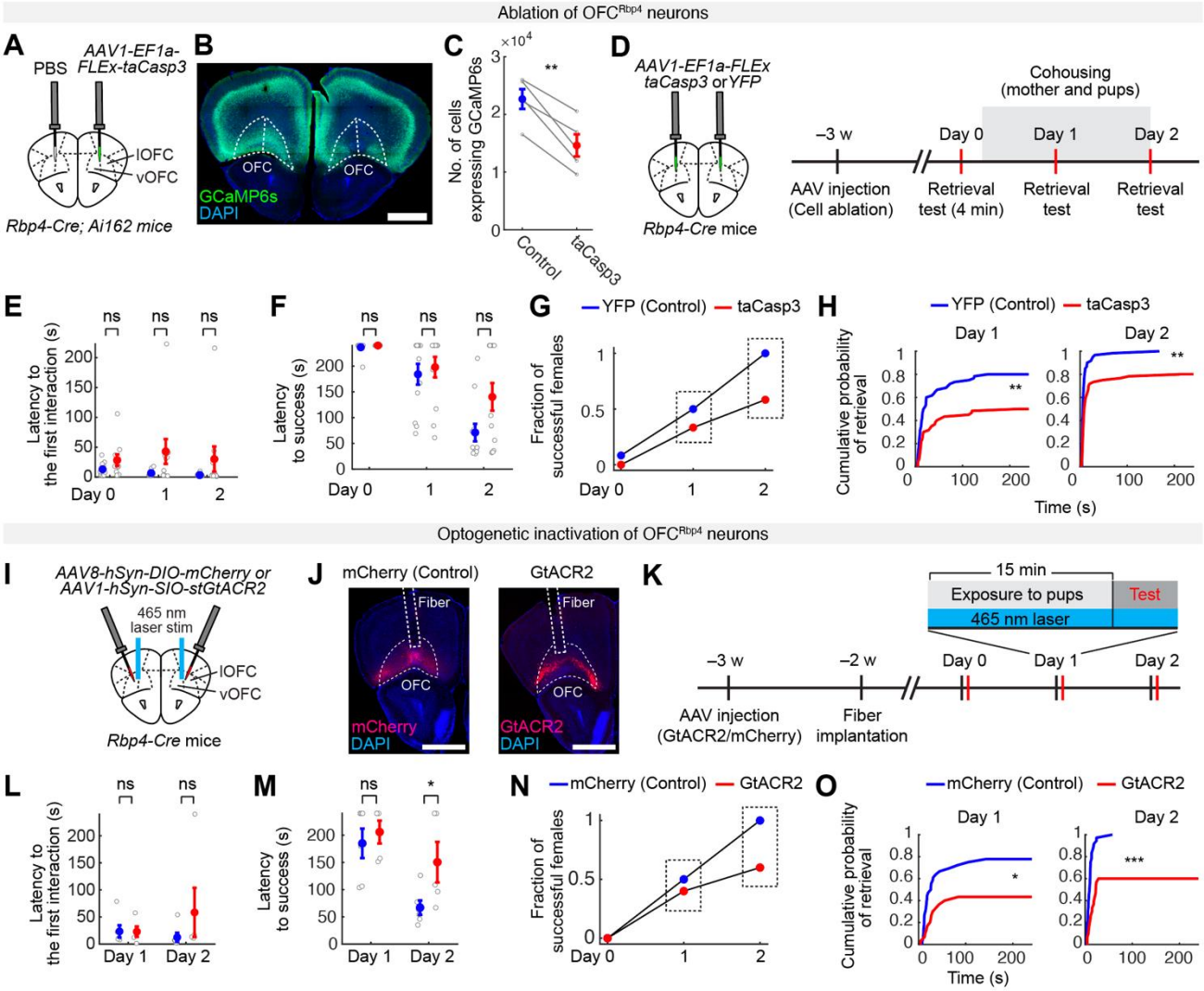

Fig. 1. Necessity of OFC^{Rbp4} neurons for effective acquisition of pup retrieval

(A) Schematic of the experimental design. AAV1 *EF1a-FLEx-taCasp3-TEVp* was injected unilaterally into the ventral and lateral OFC (vOFC and lOFC, respectively) of *Rbp4-Cre; Ai162* mice. (B) Representative coronal section showing ablation of cells only in the taCasp3-injected hemisphere. GCaMP6s signals were amplified by anti-GFP staining. Scale bar, 1 mm. (C) Quantification of the number of GCaMP6s-expressing cells in the OFC. **, $p < 0.01$ by the Wilcoxon signed-rank test (N = 5 mice). (D) Schematic of the experimental design. AAV1 *EF1a-FLEx-taCasp3-TEVp* or AAV1 *EF1a-DIO-YFP* was injected into the bilateral OFC of virgin *Rbp4-Cre* mice more than 3 weeks before the behavior assay. (E, F) Latency to the first interaction (E) and collection of all six pups in 4 min (F). ns, not significant by the Mann–Whitney *U* test (N = 10 for each group). (G) Proportion of animals that retrieved all six pups within 4 min. A significant delay was observed in taCasp3-injected animals (N = 10 mice each). (H) Cumulative probability of pup retrieval within the 4-min trial. **, $p < 0.01$ by the Kolmogorov–Smirnov test. (I) Schematic of the experimental design. AAV1 *hSyn-DIO-stGtACR2-fusionRed* or AAV8 *hSyn-DIO-mCherry* was injected into the bilateral OFC of virgin *Rbp4-Cre* mice. (J) Representative coronal section showing

the optic fiber tract and expression of mCherry (left) and stGtACR2 (right) from *Rbp4-Cre* mice. Scale bar, 1 mm. (K) Schematic of the experimental design. During the exposure period, three pups were given for 15 min, followed by the test session. The laser was kept on during both the cohousing and test sessions. (L, M) Latency to the first interaction (L) and collection of all six pups in 4 min (M). *, $p < 0.05$ by the Mann–Whitney *U* test (N = 6 for each group). (N) Proportion of animals that retrieved all six pups within 4 min. (O) Cumulative probability of pup retrieval within the 4-min trial. *, $p < 0.05$, and ***, $p < 0.001$ by the Kolmogorov–Smirnov test.

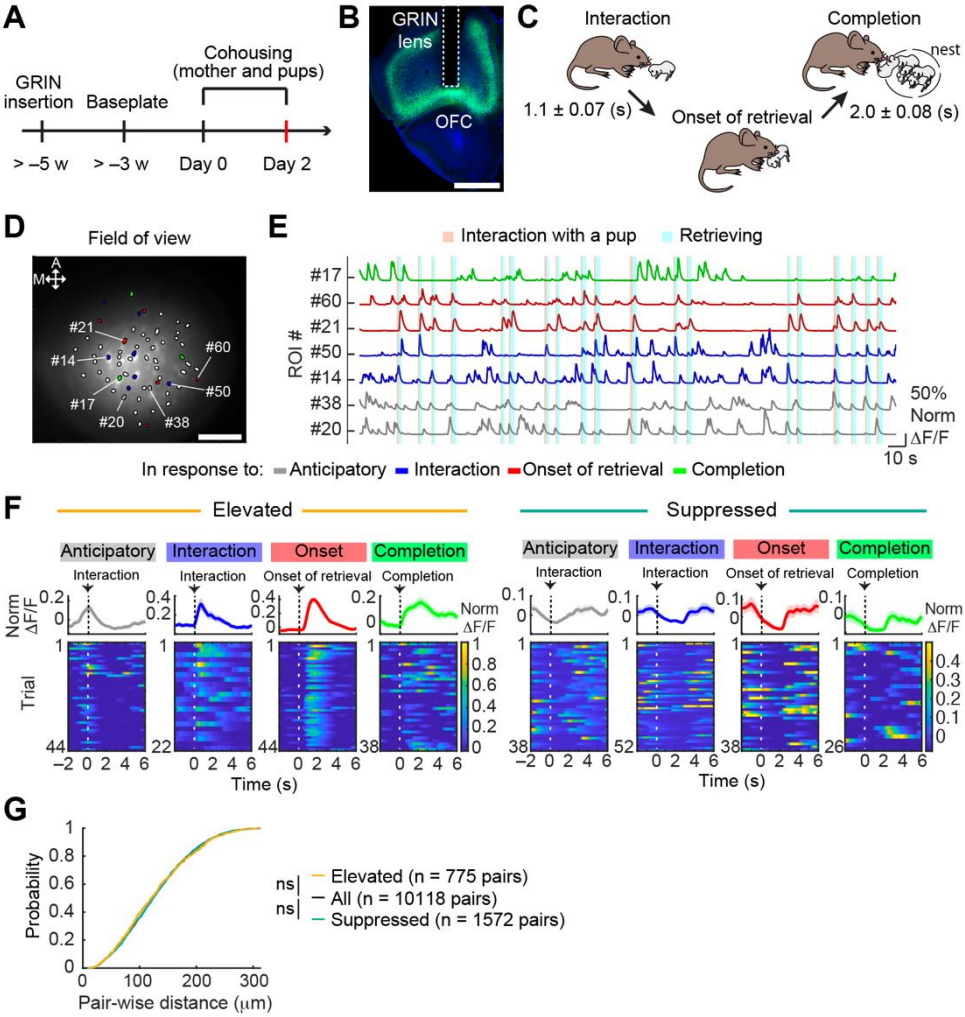

Fig. 2. Pup retrieval-related responses in OFC^{Rbp4} neurons.

(A) Schematic of the experimental timeline. (B) Representative image showing the GRIN lens tract and the expression of GCaMP6s. Scale bar, 1 mm. (C) Schematic of sequential behavioral categories during pup retrieval. The number indicates the duration between events (± standard error of the mean [SEM]) in female mice after 2 days of cohousing. (D) Example of a spatial map displaying ROIs responsive during pup retrieval in a female mouse after 2 days of cohousing. ROIs are drawn with black lines. Colors within the ROIs correspond to the elevated-response categories described in panel C: gray, anticipatory; blue, interaction; red, onset of retrieval; and green, completion. A, anterior, M, medial. Scale bar, 100 μm. (E) Examples of Ca^{2+} traces from ROIs responding to anticipatory, interaction, onset of retrieval, or completion. The indicated IDs correspond to the numbers in panel B. (F) Typical trial-average activity (top) of significantly responding individual ROIs to indicated behavioral categories, exhibiting normalized (norm) ΔF/F values to the maximum ΔF/F within each individual. Colored heat maps at the bottom show the corresponding single trials. (G) Pairwise distances between all ROIs, within elevated ROIs, and within suppressed ROIs. Data from all female mice (N = 8) on cohousing day 2 were analyzed. No clustered spatial distribution was found. ns, not significant by the Kolmogorov–Smirnov test.

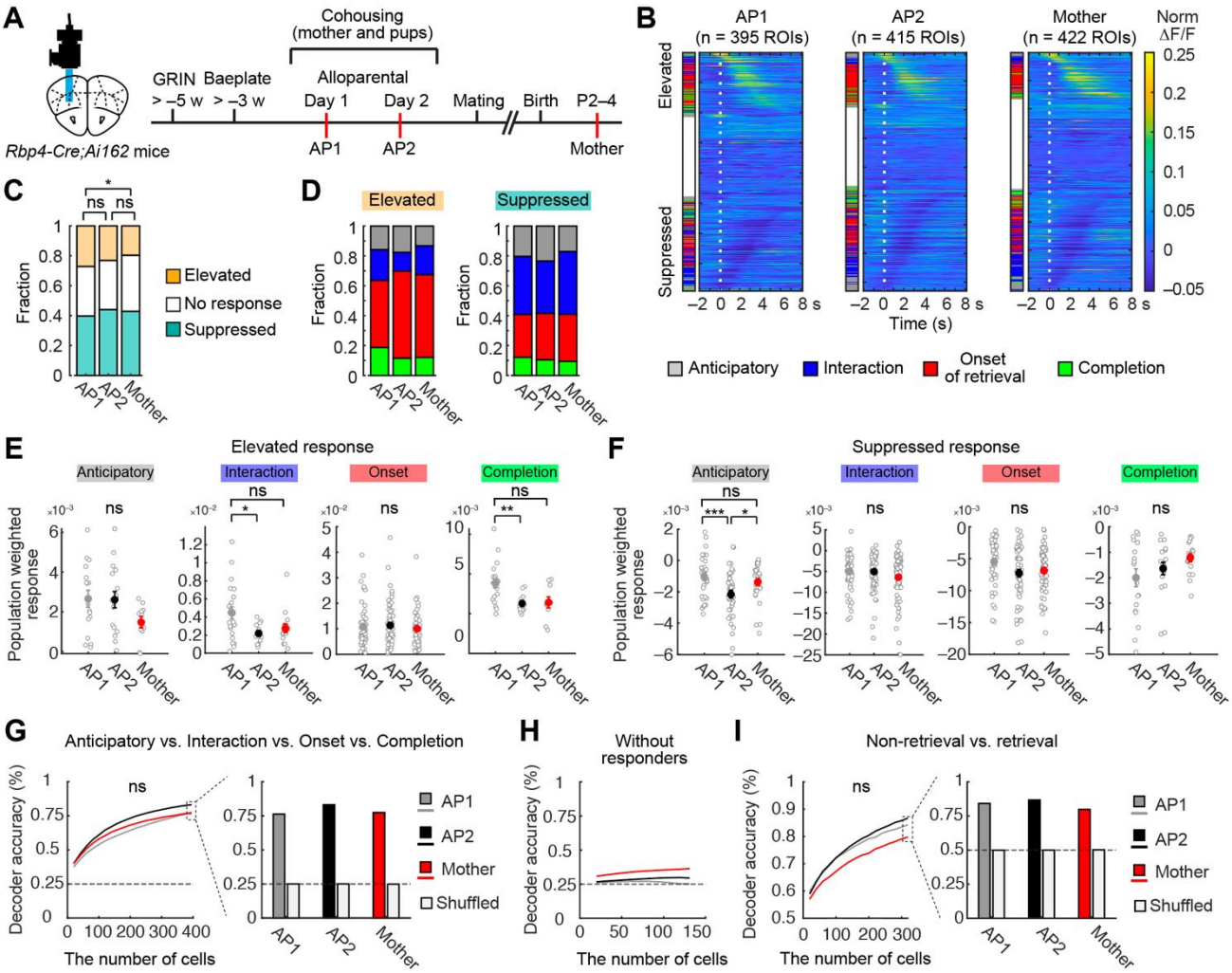

Fig. 3. A shaping representation of pup retrieval in the OFC^{Rbp4} neurons over behavioral acquisition.

(A) Schematic of the experimental paradigm. AP, alloparental day. P2–4, postpartum days 2–4. (B) Activity heat map representations showing normalized and averaged responses of individual ROIs during pup retrieval. ROIs are sorted by the time of their maximum responses on each day, with 0 indicating the timing of the interaction with a pup followed by retrieval. (C) Bar graph showing the fraction of elevated (orange) and suppressed (blue) responses during pup retrieval. *, $p < 0.05$ by the chi-square test for equality of proportions with Bonferroni correction. To normalize the statistical power among different stages, the same number of trials was used for each animal to determine whether a cell showed a significant response. (D) Fraction of cells that responded to one of the four behavioral categories of pup retrieval among the elevated (left) or suppressed (right) population. (E, F) Quantification of the population-weighted averaged response of significantly responsive cells to anticipatory, interaction, onset of retrieval, and completion (*, $p < 0.05$ by post hoc Tukey's honestly significant difference (HSD) test after a significant Kruskal–Wallis test). Error bars, SEM. (G) Classification performance of an SVM decoder. The decoder was tested for its accuracy for differentiating between any one of four different behavioral categories. The graphs indicate the mean value of accuracy across 5,000 iterations, along with the number of cells utilized for training (left).

Bar graphs indicate the SVM performance when 400 cells were utilized for training (right). The dotted line indicates the chance level. (H) Same as the left graph of (G), but the significantly responsive ROIs were excluded for training. (I) Same as (G), but the decoder was tested for its accuracy for differentiating between the non-retrieval and retrieval trials (See Methods). ns, not significant by the Kolmogorov–Smirnov test (panels G–I). Error bars, SEM. See Figs. S1–S3 for more data.

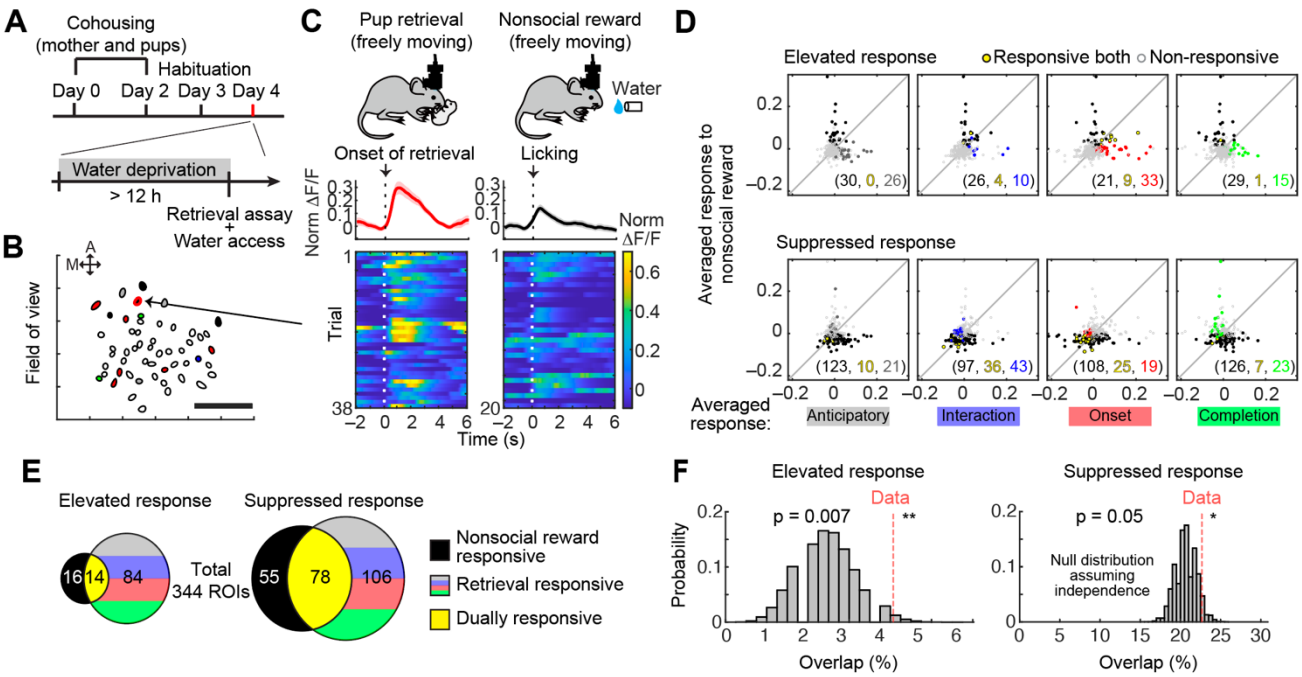

Fig. 4. Substantial overlap between OFC^{Rbp4} neurons responsive to pup retrieval and sucrose water.

(A) Schematic of the experimental paradigm. (B) Example of a spatial map of ROIs that responded during pup retrieval and passive exposure of 10% sucrose water as a nonsocial reward. A, anterior, M, medial. Scale bar, 100 µm. (C) Trial-averaged activities (top) and corresponding activity heat maps of individual trials (bottom) for a ROI responding to both the onset stage and the water reward. (D) Mean response of individual ROIs to retrieval-related activity (x-axis) and the water reward (y-axis). Colored dots indicate the ROIs that showed a significant response (n = 344 ROIs from N = 6 mice). Numbers in parentheses (*x*, *y*, *z*) indicate: *x*, the number of ROIs responsive to the nonsocial reward; *y*, the number of dually responsive ROIs; and *z*, the number of ROIs singly responsive to one of the behavioral categories. (E) Venn plots showing the number of ROIs responding to one of the behavioral categories of pup retrieval and the water reward. (F) Overlap compared with the null distribution assuming retrieval- and nonsocial reward-responsive ROIs are independent samples (*, $p < 0.05$, **, $p < 0.01$ by extreme upper-tail probability computed by binominal distribution).

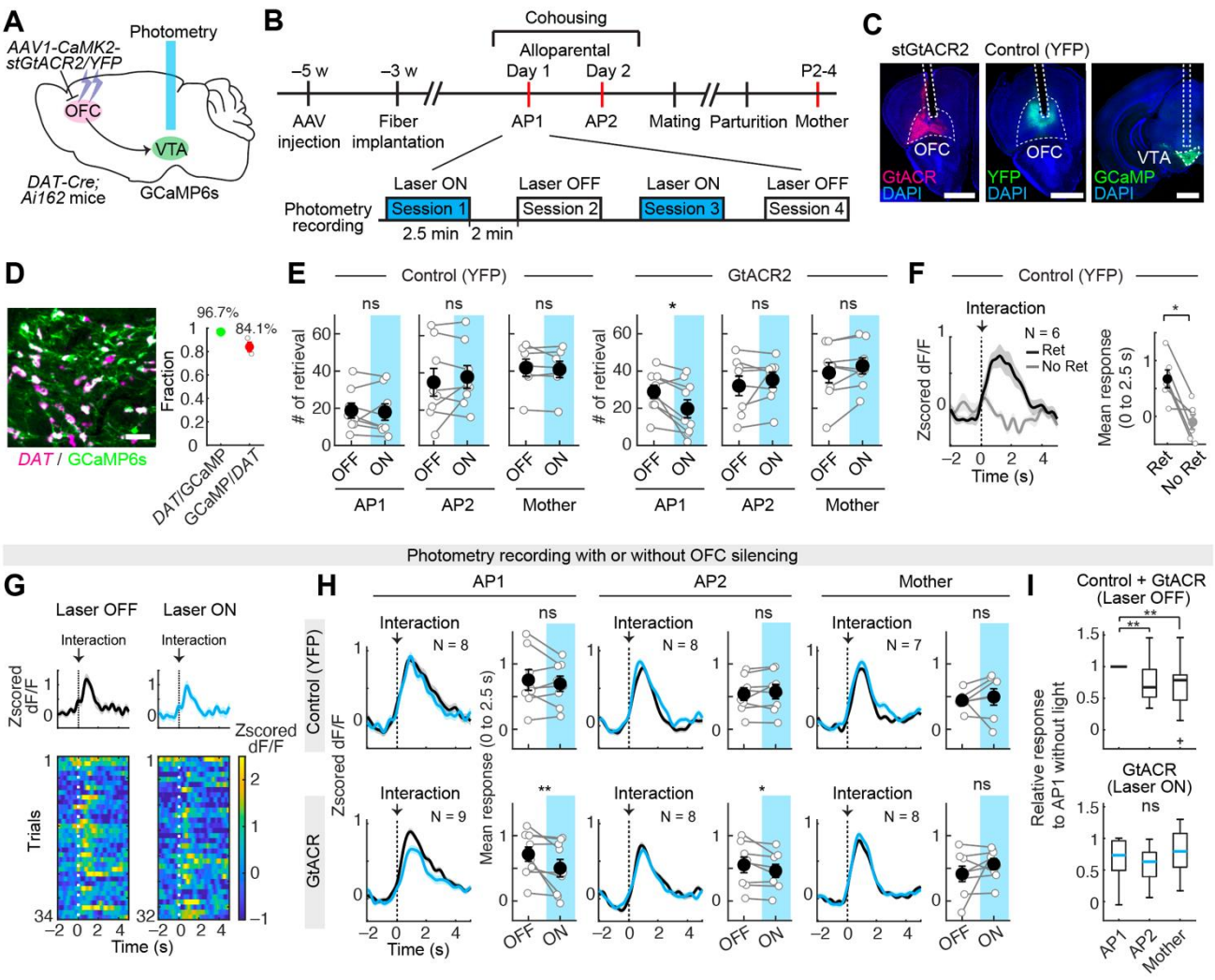

Fig. 5. The OFC facilitates pup retrieval-related activities of VTA^{DA} neurons.

(A) Schematic of the experimental design. AAV1 *CaMKII-stGtACR2-fusionRed* or AAV1 *CaMKII-YFP* was injected into the bilateral OFC of virgin *DAT-Cre; Ai162* mice. (B) Schematic of the experimental time line, including four imaging sessions (duration: 2.5 min). The first and third sessions involve laser light (blue), while the second and fourth sessions serve as internal controls without laser. (C) Representative coronal sections showing the optic fiber tract and expression of stGtACR2 (left), YFP (middle), and GCaMP6s (right) in *DAT-Cre; Ai162* mice. Scale bar, 1 mm. (D) Left: Representative coronal section showing *DAT* mRNA (magenta) and GCaMP6s (anti-GFP, green) in *DAT-Cre; Ai162* mice. Right: Quantification of specificity (*DAT*/GCaMP6s) and efficiency (GCaMP6s/*DAT*) (N = 3 mice). Scale bar, 50 μm. (E) Quantification of the number of pup retrievals during the photometry imaging sessions. N = 7–9 mice. *, $p < 0.05$ by the Wilcoxon signed-rank test. ns, not significant. (F) Left: Trial-averaged Z-scored peri-event time histograms (PETHs) of control animals during interaction followed by retrieval (Ret, black line) and non-retrieval (Not ret, gray line). Shadow represents the SEM. Right: The mean of Z-scored PETHs between 0 and 2.5 s, aligned to the interaction with a pup. *, $p < 0.05$ by the Wilcoxon signed-rank test. (G) Trial-averaged activities (top) and the corresponding activity heat maps of individual trials (bottom) of VTA^{DA} neurons during pup retrieval with and without laser-based inactivation of the OFC in an AP2 mouse.

0 indicates the timing of the interaction with a pup followed by retrieval. (H) Z-scored PETHs with (blue) and without (black) laser per group, and the mean of Z-scored PETHs between 0 and 2.5 s, aligned to the interaction with a pup. Top: YFP-injected group. Bottom: GtACR2-injected group. The number of animals is indicated in the panel. *, $p < 0.05$, and **, $p < 0.01$ by the Wilcoxon signed-rank test. ns, not significant. (I) Normalized mean response of Z-scored PETHs for pup retrieval across the AP1, AP2, and Mother stages. Data from the laser-off session in the GtACR group (N = 9 mice) and YFP group (N = 8 mice) were pooled as a control. ns, not significant, and **, $p < 0.05$ by a post hoc Tukey's HSD test following a significant Kruskal–Wallis test. See Fig. S4 for more data.

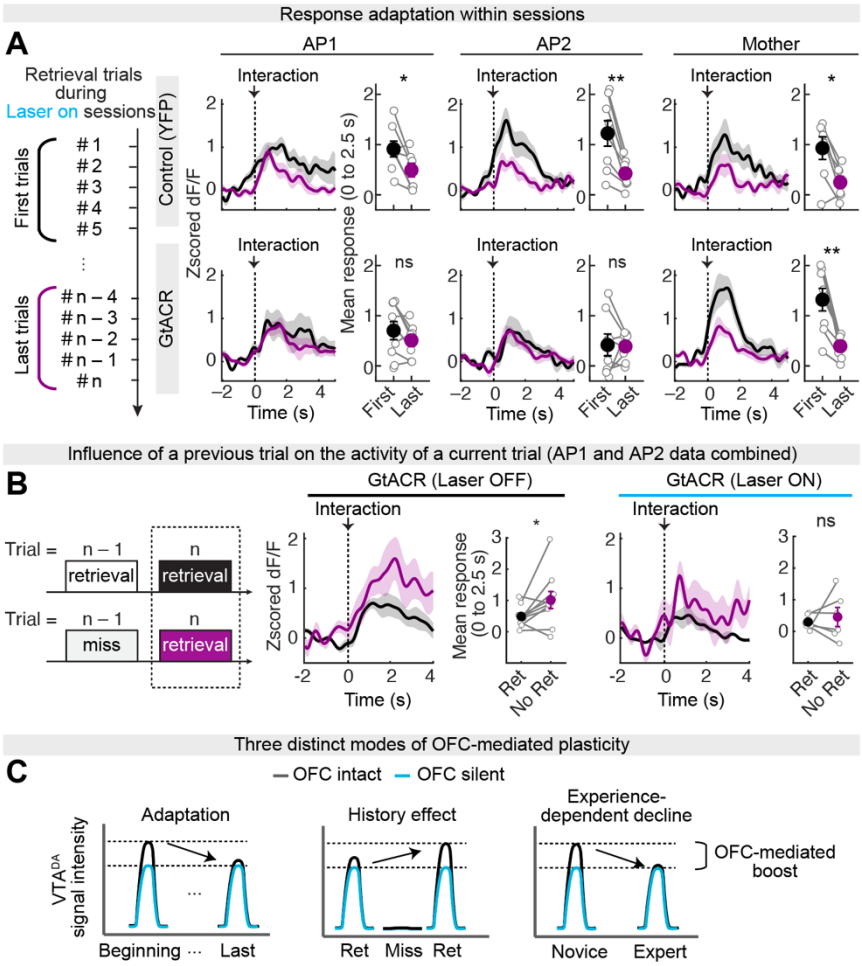

Fig. 6. The OFC regulates the dynamic modulation of VTA^{DA} neuron activity.

(A) Left: Schematic of analyzed trials. Right: Z-scored PETHs for the first (black) and last (purple) five trials during laser-on sessions for the control (top) and GtACR2 (bottom) groups. 0 indicates the timing of the interaction with a pup followed by retrieval. Shadow represents the SEM. Right graph represents the mean of Z-scored PETHs between 0 and 2.5 s, aligned to the interaction with a pup. *, $p < 0.05$, and **, $p < 0.01$ by the Wilcoxon signed-rank test. (B) Left: Schematic of analyzed trials. Middle and right: Z-scored PETHs for corresponding trials, with shadow representing the SEM, and comparisons of mean response of Z-scored PETHs between laser-off (middle, N = 10 sessions) and laser-on (right, N = 6 sessions) sessions from GtACR2-injected mice. Data from both AP1 and AP2 were pooled, utilizing mice with more than five trials. ns, not significant and *, $p < 0.05$ by the Wilcoxon signed-rank test. (C) Schematic describing three models of VTA^{DA} neuron dynamics and the contribution of the OFC. See Fig. S4 for more data.

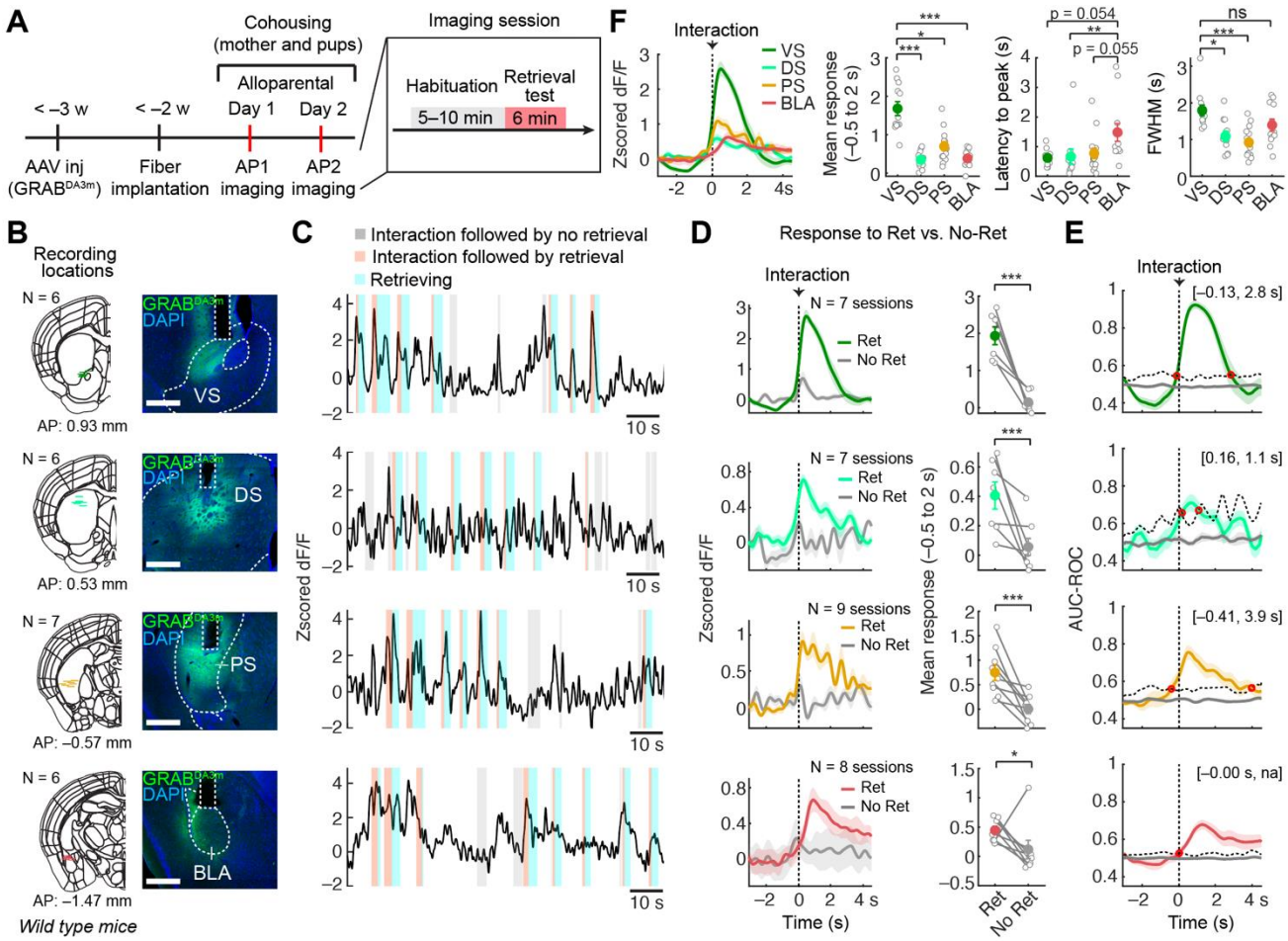

Fig. 7. DA is released in the multiple downstream targets during pup retrieval.

(A) Schematic of the experimental timeline. (B) Left: Schematics of coronal sections showing the position of the optic fiber (N = 6–7 mice each). AAV9 *hSyn-GRAB^{DA3m}* was injected into the left VS, DS, PS, or BLA of the virgin wild-type mice. Right: Representative coronal sections showing the expression of GRAB^{DA3m} without antibody staining. Scale bar, 500 μm. (C) Representative photometry trace recorded from an AP2 female during pup retrieval. Colors correspond to specific behavioral events as indicated above the panel. (D) Left: Trial-averaged Z-scored PETH traces fitted to the interaction with a pup followed by retrieval (colored) or non-retrieval (gray). Right: The mean of Z-scored PETHs between 0 and 2 s, aligned to the interaction with a pup. The number of sessions is indicated in the panel (data pooled from AP1 and AP2). *, $p < 0.05$, and ***, $p < 0.001$ by the Mann–Whitney *U* test. (E) The averaged traces of the AUC-ROC calculated for each animal. Dashed black lines display the mean +2SD of the AUC-ROC from trial-shuffled data (gray trace). Red dots indicate time points exceeding or falling below 2SD of shuffled data for the first time.

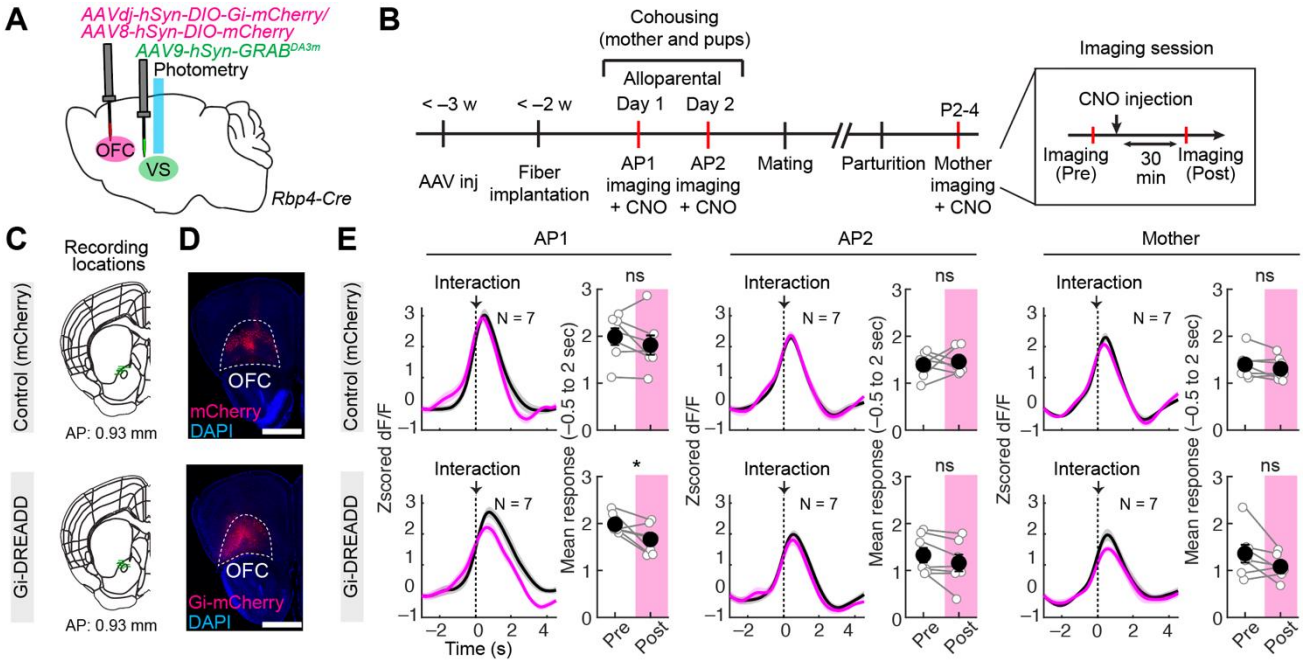

Fig. 8. The OFC regulates DA release in the VS during pup retrieval.

(A) Schematic of the experimental design. AAVdj *hSyn-DIO-Gi-mCherry* or AAV8 *hSyn-DIO-mCherry* as a control was injected into the bilateral OFC of the virgin *Rbp4-Cre* mice. AAV9 *hSyn-GRAB*^{DA3m} was injected into the left VS. (B) Schematic of the experimental time line, including an imaging session (duration: 6 min). (C) Schematics of coronal sections showing the position of the optic fiber (N = 7 mice for each group). (D) Representative coronal sections showing the expression of mCherry (top) and Gi-mCherry (bottom). Scale bar, 1 mm. (E) Z-scored PETHs before (black line) and after (magenta line) CNO administration (left), with corresponding mean responses of Z-scored PETHs. (right). Top: mCherry-injected control group. Bottom: hM4Di-injected group. The number of animals is indicated in the panel. 0 indicates the timing of the interaction. *, $p < 0.05$, by the Wilcoxon signed-rank test. ns, not significant. See Fig. S6 for schematic summary of all the data.

Supplementary Figures

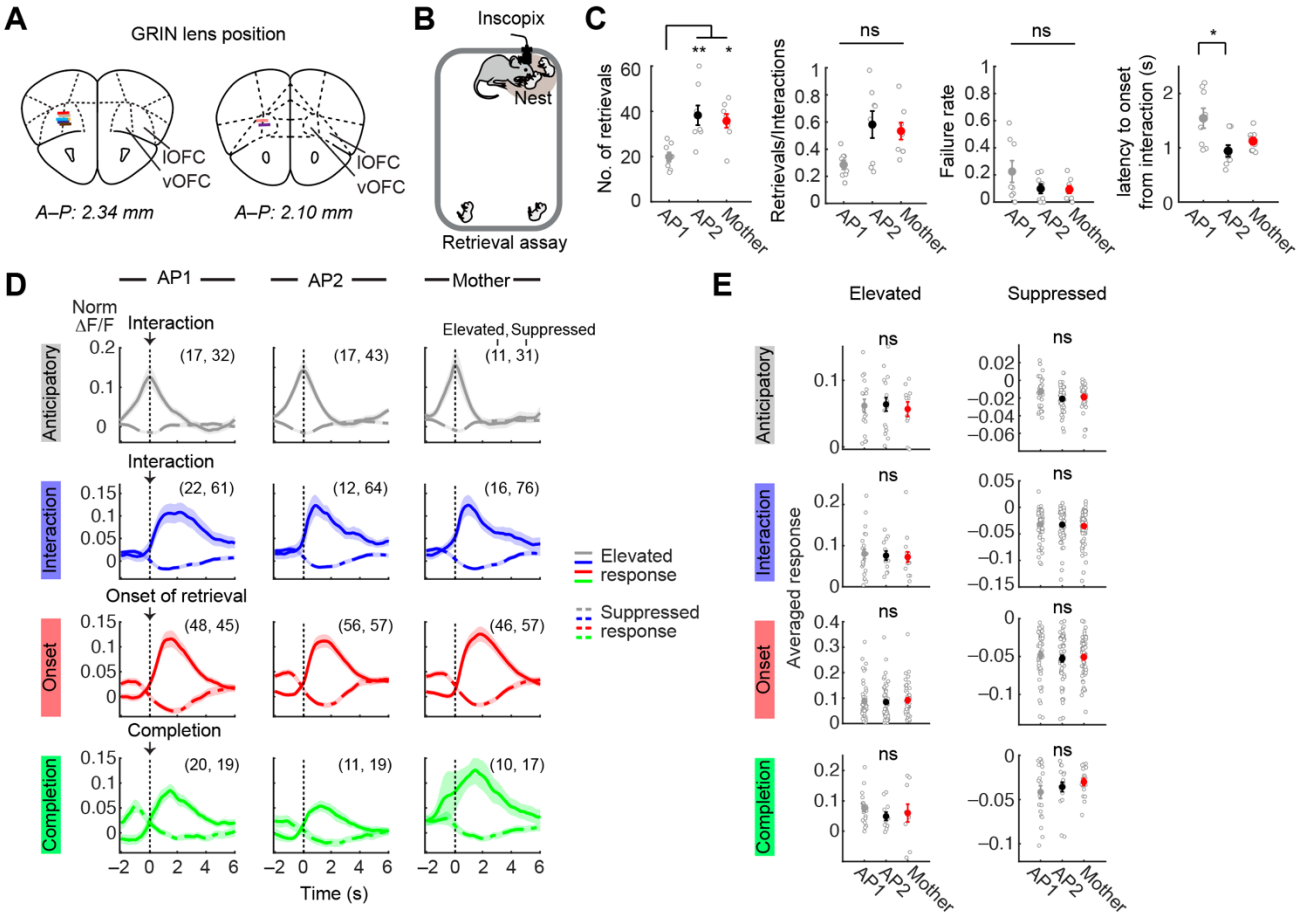

Fig. S1. More data on the neural representations of OFC^{Rbp4} neurons during pup retrieval, related to Figs. 2 and 3.

(A) Schematics of coronal sections showing the position of the GRIN lens (N = 8 mice). (B) Schematic of the pup retrieval assay during Ca^{2+} imaging. (C) Quantification of pup retrieval performance during two 6-min imaging sessions (dataset includes eight mice successfully imaged across the AP1, AP2, and Mother stages). (From left to right) Total number of pup retrievals. Success rate calculated as the number of retrievals over the number of pup interactions. Failure rate calculated as the number of incomplete retrievals (dropping before reaching the nest) normalized to the total number of retrievals. Latency to onset from interaction. *, $p < 0.05$, and **, $p < 0.01$ by a post hoc Tukey's HSD test following a significant one-way ANOVA. Error bars indicate the SEM. (D) Average activity trace of significantly responsive ROIs to anticipatory, interaction, onset of retrieval, and completion. Solid and dotted lines indicate elevated and suppressed responses, respectively. The numbers in parentheses indicate the number of cells that exhibited elevated or suppressed (sup) responses. (E) Quantification of averaged response (ns, not significant by the Kruskal–Wallis test).

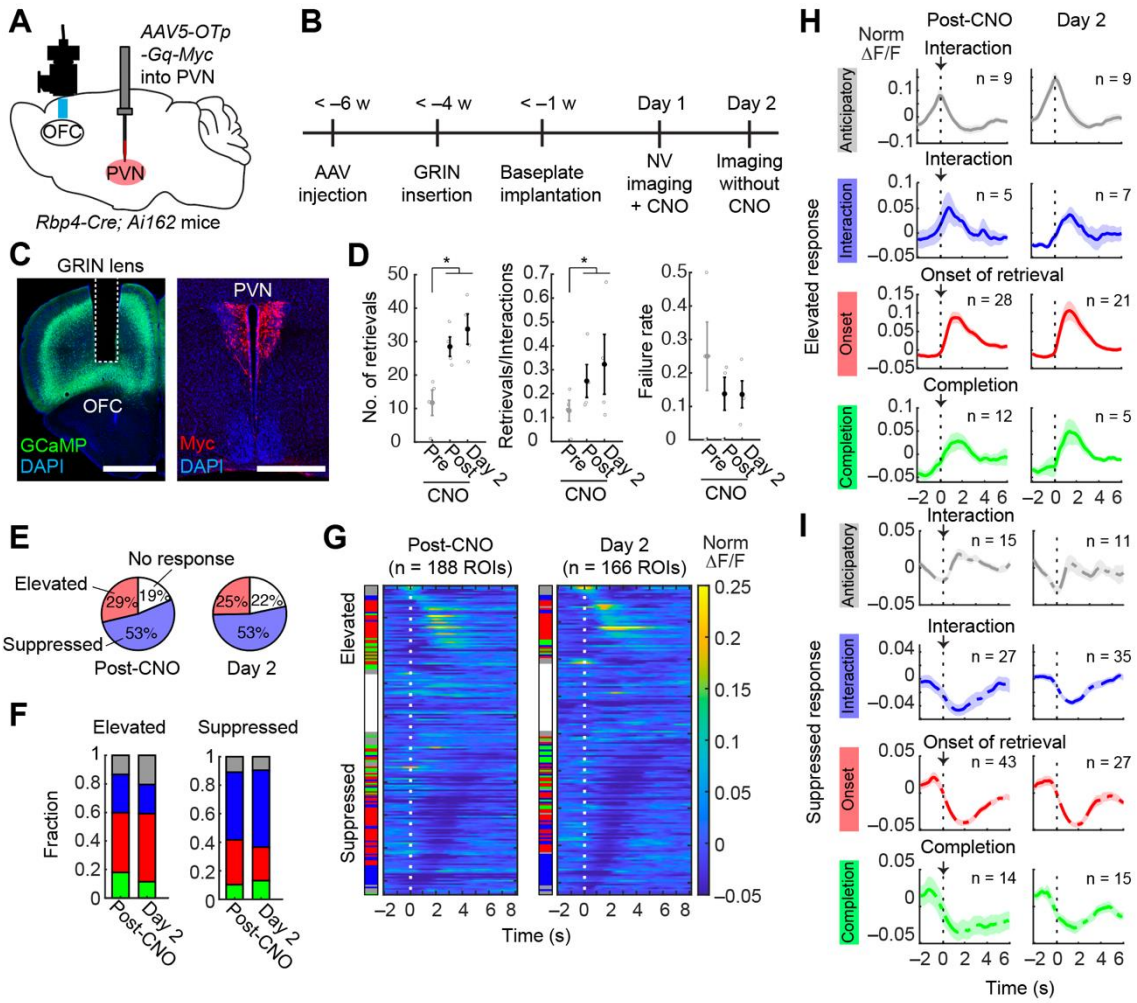

Fig. S2. Representation of pup retrieval emerges by activating OT neurons in the PVN of virgin female mice, related to Fig. 3.

(A) Schematics of the experimental design. AAV5 *OTp-hM3D(Gq)-Myc* was injected into the bilateral PVN of virgin *Rbp4-Cre; Ai162* mice. (B) Schematic of the experimental time line. (C) Representative coronal sections showing the tract of the GRIN lens in the OFC (left) and expression of Gq-Myc in the PVN (right). Scale bars, 500 μm. (D) Quantification of pup retrieval performance during the imaging sessions. Left: Number of pup retrievals. Middle: Success rate as in Figure S1B. Right: Failure rate as in Figure S1B. *, $p < 0.05$ by a post hoc Tukey's HSD test after a significant one-way ANOVA (N = 4 mice). Error bars indicate the SEM. (E) Pie charts showing the fraction of elevated (red) and suppressed (blue) responses during pup retrieval. (F) Fraction of ROIs that showed elevated (left) or suppressed (right) responses to one of the behavioral categories of pup retrieval. (G) Activity heat map representations showing normalized and averaged responses of individual ROIs during pup retrieval. 0 indicates the timing of the interaction with a pup followed by retrieval. (H, I) Averaged activity traces of significantly responsive ROIs to anticipatory, interaction, onset of retrieval, and completion of retrieval. The number of datasets is indicated in the panel.

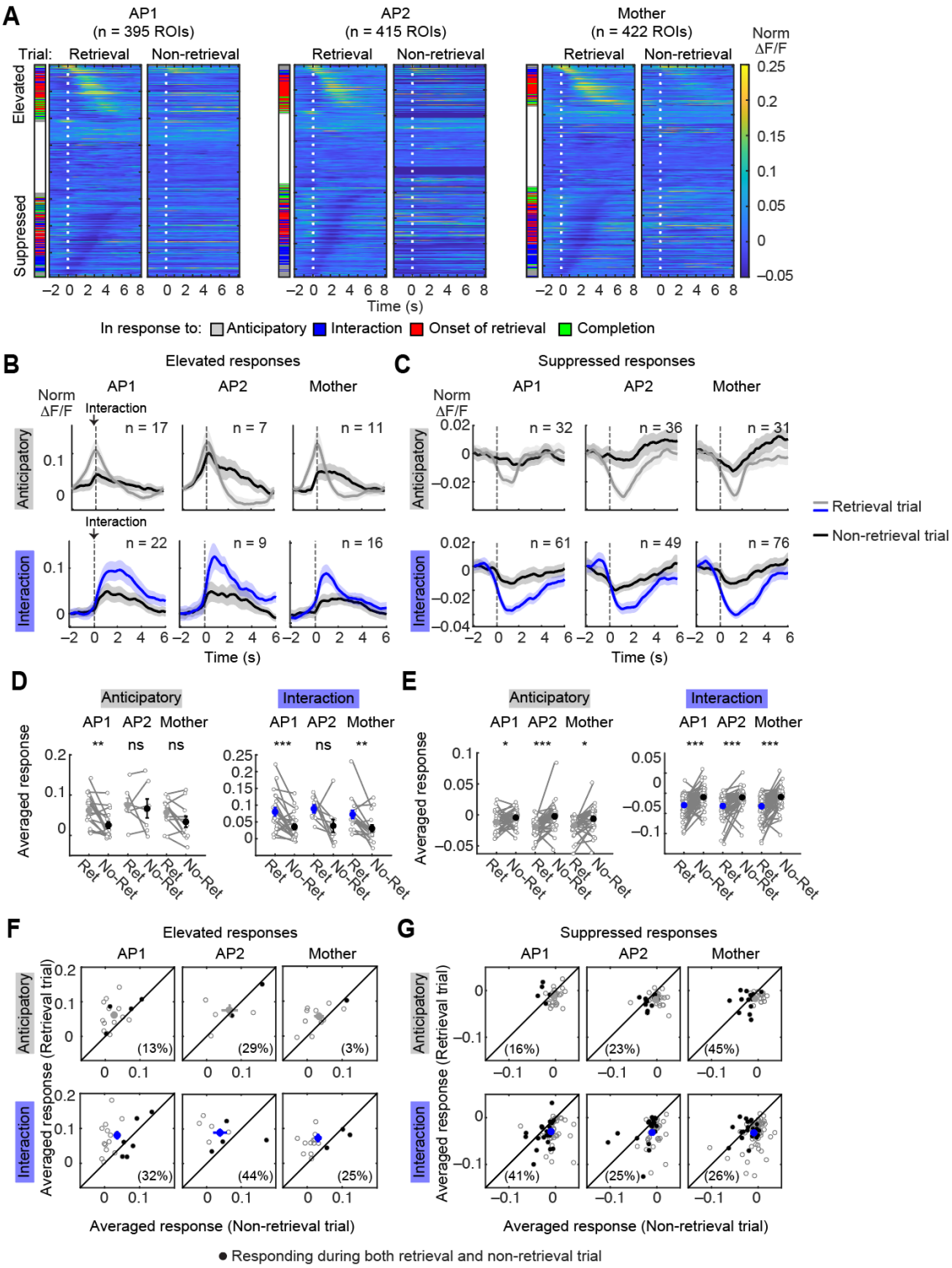

Fig. S3. The response of OFC^{Rbp4} neurons during non-retrieval trials, related to Fig. 3. (A) Activity heat map representations showing normalized and averaged responses of individual ROIs during the trials with pup retrieval (left, the same data as Fig. 3B) and interaction trials that were not followed by pup retrieval (right, "Non-retrieval"). 0 indicates the timing of the interaction with a pup. To avoid a low statistical power, data of ROIs from the mice that performed seven or fewer non-retrieval interaction trials were excluded (shown in dark blue rows). (B, C) Averaged activity trace of significantly

responsive ROIs to anticipatory and interaction from elevated (B) and suppressed (C) responses. (D, E) Quantification of averaged response. *, $p < 0.05$, **, $p < 0.01$, ***, $p < 0.001$ by the Wilcoxon signed-rank test. ns, not significant. The number of datasets is indicated in panel B or C. (F, G) Mean response during non-retrieval trials (x-axis) of individual ROIs that exhibited a significant response during the retrieval trials (y-axis). Black dots indicate the dual responders and colored dots indicate the mean value (± SEM) of the averaged response. Numbers in parentheses indicate the fraction of dual responders.

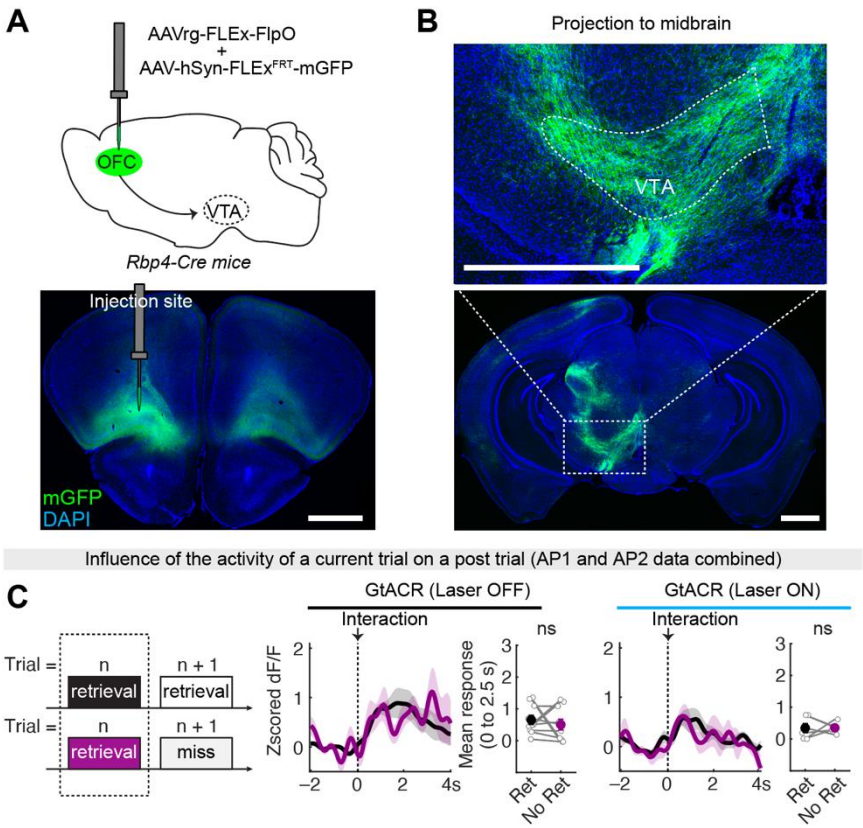

Fig. S4. OFC^{Rbp4} neurons project axons to the VTA, and additional data on pup-retrieval-related activities of VTA^{DA} neurons, related to Fig. 5 and 6.

(A) Top: Schematic of the virus injection strategy. A mixture of AAVrg *CAG-FLEx-FlpO* and AAV9 *hSyn-fDIO-mGFP* was injected into the left OFC. Bottom: Representative coronal section showing the injection site. (B) Representative coronal section showing axonal projections to the midbrain. Scale bars, 1 mm. (C) Left: Schematic of analyzed trials. Middle and right: Trial-averaged Z-scored PETHs for corresponding trials, with shadow representing the SEM, and comparisons of the mean responses of Z-scored PETHs between laser-off (middle, N = 10 sessions) and laser-on (right, N = 6 sessions) sessions from GtACR2-injected mice. Data from both AP1 and AP2 were pooled, utilizing mice with more than five trials. ns, not significant by the Wilcoxon signed-rank test.

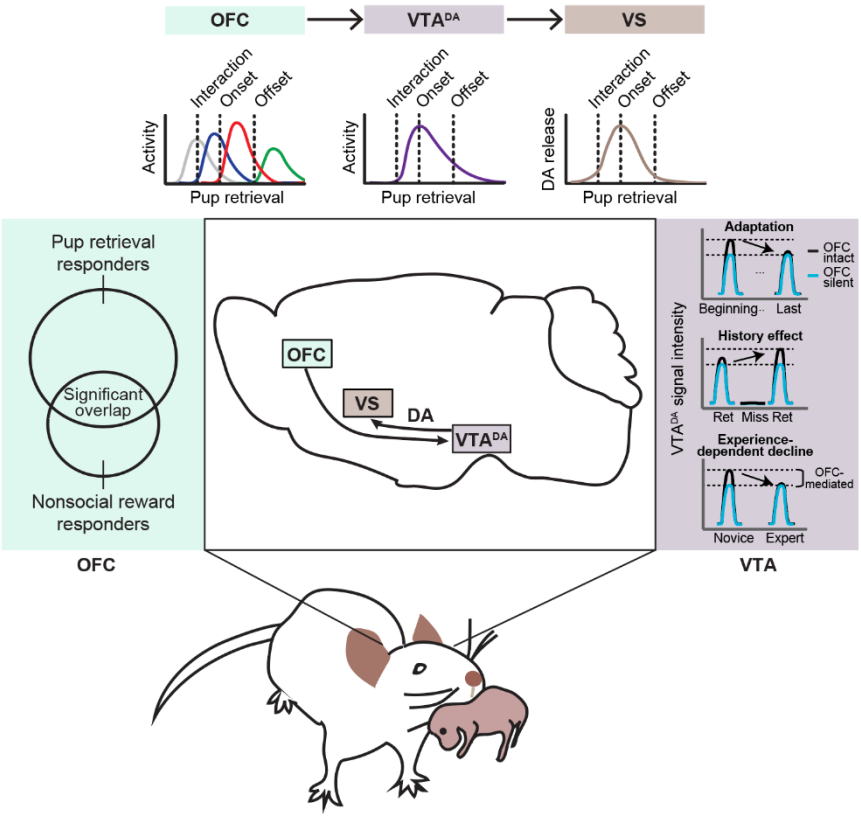

Fig. S5. Graphical abstract.

The neural representation of pup retrieval in OFC^{Rbp4} neurons significantly overlaps with those responding to nonsocial reward and cover the entire behavioral sequences. VTA^{DA} neurons, which are downstream targets of OFC^{Rbp4} neurons, show phasic activity that reaches its peak at the onset of the pup retrieval, leading to a peak in DA signals in the VS. Impairment of OFC activity disrupts the dynamic modulation of VTA^{DA} neuron activity at multiple time scales. We propose that OFC activity, especially during the anticipatory and interaction categories, provides top-down facilitatory signals to VTA^{DA} neurons in the early phase of acquiring alloparental behavior.

Table S1. Statistical summary. All tests were two-tailed.

	group	subgroup	pair	test	p-value	p-value after Bonferroni correction
Fig. 1C			Control vs taCasp3	paired ttest	0.0039	
Fig. 1E		Day 0	YFP vs taCasp3	ranksum	0.1715	
		Day 1	YFP vs taCasp3	ranksum	0.1104	
		Day 2	YFP vs taCasp3	ranksum	0.5571	
Fig. 1F		Day 0	YFP vs taCasp3	ranksum	0.3681	
		Day 1	YFP vs taCasp3	ranksum	0.3849	
		Day 2	YFP vs taCasp3	ranksum	0.1288	
Fig. 1H		Day 1	YFP vs taCasp3	ks-test	0.0036	
		Day 2	YFP vs taCasp3	ks-test	0.0068	
Fig. 1L		Day 1	mCherry vs GtACR2	ranksum	0.6623	
		Day 2	mCherry vs GtACR2	ranksum	0.0519	
Fig. 1M		Day 1	mCherry vs GtACR2	ranksum	0.697	
		Day 2	mCherry vs GtACR2	ranksum	0.0476	
Fig. 1O		Day 1	mCherry vs GtACR2	ks-test	0.0309	
		Day 2	mCherry vs GtACR2	ks-test	2.50E-05	
Fig. 2G			Elevated vs All	ks test	0.3476	
			Suppressed vs All	ks test	0.9754	
Fig. 3C			AP1 vs AP2	Chi-square	0.1941	
			AP1 vs Mother	Chi-square	0.121	0.363
			AP2 vs Mother	Chi-square	0.2217	
Fig. 3E	Elevated	Anticipatory		Kruskal-Wallis	0.1262	
		Interaction		Kruskal-Wallis	0.038	
			AP1 vs AP2	Tukey's post-hoc	0.0497	
			AP1 vs Mother	Tukey's post-hoc	0.1552	
			AP2 vs Mother	Tukey's post-hoc	0.8105	
		Onset		Kruskal-Wallis	0.8282	
		Completion		Kruskal-Wallis	0.0043	
			AP1 vs AP2	Tukey's post-hoc	0.0063	
			AP1 vs Mother	Tukey's post-hoc	0.0678	
			AP2 vs Mother	Tukey's post-hoc	0.7877	
Fig. 3F	Suppressed	Anticipatory		Kruskal-Wallis	0.002	
			AP1 vs AP2	Tukey's post-hoc	0.0021	

			AP1 vs Mother	Tukey's post-hoc	0.5939
			AP2 vs Mother	Tukey's post-hoc	0.0459
		Interaction		Kruskal-Wallis	0.1433
		Onset		Kruskal-Wallis	0.0688
		Completion		Kruskal-Wallis	0.1351
Fig. 4F		Elevated	Data vs simulated-distribution	extreme upper-tail probability	0.007
		Suppressed	Data vs simulated-distribution	extreme upper-tail probability	0.05
Fig. 5E	Control	AP1	ON vs OFF	signed-rank	0.5312
		AP2	ON vs OFF	signed-rank	1
		Mother	ON vs OFF	signed-rank	0.8281
	GtACR2	AP1	ON vs OFF	signed-rank	0.0156
		AP2	ON vs OFF	signed-rank	0.625
		Mother	ON vs OFF	signed-rank	0.1562
Fig. 5F			Ret vs Non-Ret	signed-rank	0.0312
Fig. 5H	Control	AP1	ON vs OFF	signed-rank	0.7422
		AP2	ON vs OFF	signed-rank	0.4609
		Mother	ON vs OFF	signed-rank	0.375
	GtACR2	AP1	ON vs OFF	signed-rank	0.0078
		AP2	ON vs OFF	signed-rank	0.0234
		Mother	ON vs OFF	signed-rank	0.1953
Fig. 5I		OFF		Kruskal-Wallis	0.0004
			AP1 vs AP2	Tukey's post-hoc	0.0029
			AP1 vs Mother	Tukey's post-hoc	0.0015
			AP2 vs Mother	Tukey's post-hoc	0.9688
		ON		Kruskal-Wallis	0.5518
Fig. 6A	Control	AP1	First vs Last	signed-rank	0.0469
		AP2	First vs Last	signed-rank	0.0078
		Mother	First vs Last	signed-rank	0.0312
	GtACR2	AP1	First vs Last	signed-rank	0.1484
		AP2	First vs Last	signed-rank	0.8438
		Mother	First vs Last	signed-rank	0.0078
Fig. 6B		OFF	Ret vs Non-Ret	signed-rank	0.0371
		ON	Ret vs Non-Ret	signed-rank	1

Fig. 7D		VS	Ret vs Non-Ret	signed-rank	0.0006
		DS	Ret vs Non-Ret	signed-rank	0.0059
		PS	Ret vs Non-Ret	signed-rank	0.0005
		BLA	Ret vs Non-Ret	signed-rank	0.0104
Fig. 7F		Mean response		Kruskal-Wallis	3.88E-06
			VS vs DS	Tukey's post-hoc	1.88E-05
			VS vs PS	Tukey's post-hoc	0.01859
			VS vs BLA	Tukey's post-hoc	5.60E-05
			DS vs PS	Tukey's post-hoc	0.1952
			DS vs BLA	Tukey's post-hoc	0.9877
			PS vs BLA	Tukey's post-hoc	0.3345
		Latency to Peak		Kruskal-Wallis	0.0049
			VS vs DS	Tukey's post-hoc	0.8038
			VS vs PS	Tukey's post-hoc	0.9996
			VS vs BLA	Tukey's post-hoc	0.0541
			DS vs PS	Tukey's post-hoc	0.7284
			DS vs BLA	Tukey's post-hoc	0.004
			PS vs BLA	Tukey's post-hoc	0.0552
		FWHM		Kruskal-Wallis	0.0009
			VS vs DS	Tukey's post-hoc	0.0211
			VS vs PS	Tukey's post-hoc	0.0007
			VS vs BLA	Tukey's post-hoc	0.3312
			DS vs PS	Tukey's post-hoc	0.8693
			DS vs BLA	Tukey's post-hoc	0.6105
			PS vs BLA	Tukey's post-hoc	0.1576
Fig. 8E	Control	AP1	Pre vs Post	signed-rank	0.2969
		AP2	Pre vs Post	signed-rank	0.6875
		Mother	Pre vs Post	signed-rank	0.2188
	Gi-DREADD	AP1	Pre vs Post	signed-rank	0.0312
		AP2	Pre vs Post	signed-rank	0.0781
		Mother	Pre vs Post	signed-rank	0.0781
Fig. S1C	# of retrieval			one-way ANOVA	0.0171
			Day1 vs Day2	Tukey's post-hoc	0.0278
			Day1 vs Mother	Tukey's post-hoc	0.0378
			Day2 vs Mother	Tukey's post-hoc	0.9887

	Retrievals/Interactions			one-way ANOVA	0.2224
	Failure rate			one-way ANOVA	0.3622
	latency to onset			one-way ANOVA	0.0218
			Day1 vs Day2	Tukey's post-hoc	0.0262
			Day1 vs Mother	Tukey's post-hoc	0.0669
			Day2 vs Mother	Tukey's post-hoc	0.8944
Fig. S1E	Elevated	Anticipatory		Kruskal-Wallis	0.8993
		Interaction		Kruskal-Wallis	0.897
		Onset		Kruskal-Wallis	0.8374
		Completion		Kruskal-Wallis	0.5026
	Suppressed	Anticipatory		Kruskal-Wallis	0.115
		Interaction		Kruskal-Wallis	0.7329
		Onset		Kruskal-Wallis	0.5248
		Completion		Kruskal-Wallis	0.7703
Fig. S2D	# of retrieval			one-way ANOVA	0.0066
			Pre vs Post		0.0294
			Pre vs Day2		0.0066
			Post vs Day2		0.6056
	Retrievals/Interactions			one-way ANOVA	0.321
	Failure rate			one-way ANOVA	0.4453
Fig. S3D	Elevated	Anticipatory	AP1	signed-rank	0.0036
			AP2	signed-rank	0.8125
			Mother	signed-rank	0.1475
		Interaction	AP1	signed-rank	0.0009
			AP2	signed-rank	0.0742
			Mother	signed-rank	0.0045
	Suppressed	Anticipatory	AP1	signed-rank	0.0287
			AP2	signed-rank	0.0001
			Mother	signed-rank	0.0151
		Interaction	AP1	signed-rank	2.25E-06
			AP2	signed-rank	1.55E-05
			Mother	signed-rank	1.27E-08
Fig. S4C		OFF	Ret vs No-Ret	signed-rank	0.4316
		ON	Ret vs No-Ret	signed-rank	1

Materials and Methods

Animals

All animals were housed under a regular 12-h dark/light cycle with *ad libitum* access to food and water. Wild-type FVB mice were purchased from CLEA Japan, Inc. (Tokyo, Japan) for backcrossing. *DAT-Cre* (Jax# 006660) and *Ai162* (*TIT2L-GC6s-ICL-tTA2*, Jax#031562) were purchased from the Jackson Laboratory. *Rbp4-Cre* mice were originally obtained from the Mutant Mouse Regional Resource Center. We used the F1 hybrid of C57BL/6 and FVB strain for all experiments. *Rbp4-Cre* heterozygous female mice (age range, 2–5 months) were used for ablation experiments using taCasp3, optogenetic silencing experiments using GtACR2, and chemogenetic silencing experiments with photometry recording of DA dynamics using $GRAB^{DA}$. *Rbp4-Cre; Ai162* double heterozygous female mice (age range, 2–6 months) were used for *in vivo* microendoscopic imaging of the OFC. *DAT-Cre; Ai162* double heterozygous female mice (age range, 2–6 months) were used for the fiber photometry experiments. Wild-type female mice (age range, 2–5 months) were used for the fiber photometry recordings of DA dynamics. To investigate maternal caregiving behaviors, this study exclusively utilized female mice. A similar study involving male mice will be detailed in future publications.

Viral preparations

The following AAV vectors were generated by Addgene.

AAV serotype 1 *EF1a-FLEx-taCasp3-TEVp* (5.8×10^{12} gp/mL) (Addgene #45580)(*44*)
AAV serotype 5 *EF1a-DIO-YFP* (1.3×10^{13} gp/mL) (Addgene #27056)
AAV serotype 8 *hSyn-DIO-mCherry* (2.2×10^{13} gp/mL) (Addgene #50459)
AAV serotype 1 *CaMK2a-stGtACR2-FusionRed* (1.3×10^{13} gp/mL) (Addgene #105669) (*73*)
AAV serotype 1 *hSyn-SIO-stGtACR2-FusionRed* (1.9×10^{13} gp/mL) (Addgene #105677) (*73*)
AAV serotype 1 *CaMK2a-EYFP* (1.0×10^{13} gp/mL) (Addgene #105622)

The following AAV vectors were generated by the UNC viral core.

AAV serotype 5 *OTp-hM3Dq-Myc* (2.9×10^{12} gp/mL) (Corresponding plasmid: Addgene #184753) (*47*)

AAV serotype 9 *hSyn-FLEx(FRT)-mGFP* (7.4×10^{12} gp/mL) (Corresponding plasmid: Addgene #71761) (*36*)

The following AAV vectors were generated by WZ Biosciences.

AAV serotype 9 $hSyn\text{-}GRAB^{DA3m}$ (2.2×10^{13} gp/mL)

pAAV CAG-FLEx-FLPo was constructed by in-fusion-based PCR cloning utilizing the following two DNA fragments: i) SalI-AscI restriction fragment of *pAAV CAG-FLEx-TCb* (Addgene #48332) as a vector backbone, and ii) PCR fragment of *FLPo* originated from *pTCAV-FLEx-FLPo* (#67829,

Addgene). Because a nuclear localization signal (NLS) was not included in this version of the *FLPo* cassette, subsequently, we performed PCR-based subcloning of SV40 NLS to the 5' end of the *FLPo* cassette, resulting in the construction of *pAAV CAG-FLEx-FLPo*. With this plasmid, the AAV serotype retro *CAG-FLEx-FlpO* (5.5×10^{12} gp/mL) was generated by the National Institute for Physiological Science viral vector core facility. The AAV serotype DJ *hSyn-DIO-hM4Di-mCherry* (6.9×10^{12} gp/mL) was generated by the Fukushima Medical University School of Medicine Viral Vector Core facility with the corresponding plasmid (Addgene #44362).

Stereotaxic injection

For targeting AAV or rabies virus into a certain brain region, stereotaxic coordinates were first defined for each brain region based on the Allen Brain Atlas (*74*). Mice were anesthetized with 65 mg/kg ketamine (Daiichi-Sankyo) and 13 mg/kg xylazine (Sigma-Aldrich) via intraperitoneal injection and head-fixed to the stereotaxic equipment (RWD). For the ablation experiments (Figure 1A–G), 200 nL of AAV1 *EF1a-FLEx-taCasp3-TEVp* was injected into the right hemisphere or bilateral OFC (coordinates relative to the bregma: anteroposterior [AP] 2.5 mm, mediolateral [ML] 1.2 mm, dorsoventral from the brain surface [DV] 1.9 mm) at a speed of 50 nL/min using a UMP3 pump regulated by Micro-4 (World Precision Instruments). For the optogenetic silencing experiments (Fig. 1I–O), 200 nL of AAV1 *hSyn-SIO-stGtACR2-FusionRed* or AAV8 *hSyn-DIO-mCherry* was injected into the bilateral OFC. To activate OT neurons in the PVN (Fig. S2), 200 nL of AAV5 *OTp-hM3D(Gq)-Myc* was injected into the bilateral PVN (coordinates relative to the bregma: AP –0.5 mm, ML 0.2 mm, DV 4.4 mm). For the optogenetic experiments with photometry recordings (Fig. 5), 200 nL of AAV1 *CaMK2a-stGtACR2-FusionRed* or AAV1 *CaMK2a-EYFP* was injected into the bilateral OFC. For anterograde tracing from the OFC (Fig. S4A and B), 100 nL of a 1:1 mixture of AAVretro *CAG-FLEx-FlpO* and AAV9 *hSyn-FLEx(FRT)-mGFP* was injected into the left OFC. Of note, we utilized this AAVretro *CAG-FLEx-FlpO* just to drive FlpO into the injection site and did not intend its retrograde transductions. For the photometry recording of DA dynamics (Fig. 7), 200 nL of AAV9 *hSyn-GRAB^{DA3m}* was injected into the VS (coordinates relative to the bregma: AP 1.6 mm, ML 1.2 mm, DV 4.0 mm), DS (coordinates relative to the bregma: AP 1.0 mm, ML 1.9 mm, DV 2.7 mm), PS (coordinates relative to the bregma: AP –0.4 mm, ML 3.0 mm, DV 3.55 mm), or BLA (coordinates relative to the bregma: AP –0.8 mm, ML 3.1 mm, DV 4.4 mm). For the pharmacogenetic experiments with photometry recordings (Fig. 8), 200 nL of AAVdj *hSyn-DIO-hM4Di-mCherry* or AAV8 *hSyn-DIO-mCherry* was injected into the bilateral OFC, and 200 nL of AAV9 *hSyn-GRAB^{DA3m}* was injected into the VS. After viral injection, the incision was sutured, and the animal was warmed using a heating pad to facilitate recovery from anesthesia. The animal was then returned to the home cage.

Histology and histochemistry

Mice were given an overdose of isoflurane and perfused transcardially with PBS followed by 4%

paraformaldehyde (PFA) in PBS. Brain tissues were post-fixed with 4% PFA in PBS overnight at 4 °C, cryoprotected with 30% sucrose solution in PBS at 4 °C for 24–48 h, and embedded in O.C.T. compound (Tissue-Tek, cat#4583). For immunostaining of GFP (Fig. S4), GCaMP6s (Figs. 1, 2, 5, and S2), YFP (Fig. 5), and Myc-tag (Fig. S2), we collected 40-μm coronal sections of the brain using a cryostat (model #CM1860; Leica). Free-floating slices were then incubated in the following solutions with gentle agitation at room temperature: 2 h in blocking solution (5% heat-inactivated goat serum, 0.4% Triton-X100 in PBS); overnight at room temperature in primary antibody 1:1000 mouse anti-GFP (GFP-1010, Aves Labs), or anti-Myc (Santa Cruz, Cat #sc-40, RRID: AB_627268) in blocking solution; 2–3 h in secondary antibody 1:500 anti-chicken-IgY Alexa488-conjugated, or goat anti-rat-IgG Cy3-conjugated or goat (Jackson ImmunoResearch) in blocking solution; 15 min in 2.5 μg/mL of DAPI (Santa Cruz, Cat #sc-3598) in PBS. Sections were mounted on slides and cover-slipped with mounting media (Fluoro-gold). Expression of stGtACR2-FusionRed (Fig. 1 and 5) or hM4Di-mCherry (Fig. 8) was detected through epifluorescence using the Cy3 filter without immunostaining. The expression of $GRAB^{DA3m}$ was detected through epifluorescence using the GFP filter without immunostaining.

Sections were imaged using an Olympus BX53 microscope with a 4× (NA 0.16) or 10× (NA 0.4) objective lens equipped with a cooled CCD camera (DP80; Olympus) or Zeiss Axio Scan.Z1 with a 10× (NA 0.45) objective lens. Every third, a total of five coronal brain sections were analyzed for quantification (Fig. 1C).

Fluorescent *in situ* hybridization (ISH)

Fluorescent ISH was performed as previously described (*75*). In brief, mice were anesthetized with sodium pentobarbital and perfused with PBS followed by 4% PFA in PBS. The brain was post-fixed with 4% PFA overnight. Thirty-micron coronal brain sections were made using a cryostat (Leica) and placed on MAS-coated glass slides (Matsunami). To generate cRNA probes, DNA templates were amplified by PCR from the C57BL/6j mouse genome or whole-brain cDNA (Genostaff, cat#MD-01). A T3 RNA polymerase recognition site (5'-AATTAACCCTCACTAAAGGG) was added to the 3' end of the reverse primers. The primer sets to generate DNA templates for cRNA probes were as follows (the first one, forward primer, the second one, reverse primer):

DAT 5'-TGCTGGTCATTGTTCTGCTC; 5'-ATGGAGGATGTGGCAATGAT

DNA templates (500–1000 ng) amplified by PCR were subjected to *in vitro* transcription with DIG (cat#11277073910)-RNA labeling mix and T3 RNA polymerase (cat#11031163001) according to the manufacturer's instructions (Roche Applied Science).

For ISH combined with anti-GFP staining, after hybridization and washing, sections were incubated with horseradish peroxidase-conjugated anti-DIG (Roche Applied Science cat#11207733910, 1:500) and anti-GFP (Aves Labs cat#GFP-1020, 1:500) antibodies overnight. Signals were amplified by TSA-plus Cyanine 3 (AKOYA Bioscience, NEL744001KT, 1:70 in 1× plus amplification diluent) for 25 min, followed by washing, and then GFP-positive cells were

visualized by anti-chicken Alexa Fluor 488 (Jackson Immuno Research cat#703-545-155, 1:250).

Pup retrieval assay

For the ablation experiment in Figure 1A–H, animals were placed in their home cage (191 × 376 × 163 mm) with standard wood chip bedding more than a day before the retrieval assay on experimental day 0. The retrieval assay was initiated by introducing two pups (Postnatal days 1–3 at experimental day 0) in opposite corners of the nest. If the two pups were successfully retrieved, another two pups were placed in the same corners. This process continued until a total of six pups were collected or a 4-min time-out occurred. Following the retrieval assay on experimental day 0, the tested virgin female was transferred to the cage of a mother and pups to initiate cohousing. On experimental days 1 and 2, the cohoused mother and pups were temporally removed, and the assay began after a 5–10-min wait. The same mother and pups were consistently used for both the assay and cohousing across different experimental days. For example, pups of postnatal day 3 were used for the experimental day 2, if pups of postnatal day 1 were used for the experimental day 0.

For the optogenetic experiment in Figure 1I–O, animals were placed in their small-sized home cage (191 × 188 × 163 mm) with standard wood chip bedding more than a day before the retrieval assay on experimental day 0. To habituate animals to the experimental setup, they were tethered with a patch cable (NA = 0.5, core diameter = 200 μm, TH200FL1A, Thorlabs) for 5–10 min. This habituation process was repeated more than twice before the experimental day 0. On the experimental day, the patch cable was connected to the animal, followed by a 5–10-min wait before laser illumination (IOS-465, RWD), adjusted to 5 mW/mm^2 at each tip of the optic fiber. Immediately after the laser illumination, three pups were introduced at the three different corners, avoiding the corner where the nest had been built. After 15 min of pup exposure, a pup was removed and two pups were left in the nest. Subsequently, a retrieval assay was performed following the same procedure as described above. The same pups (postnatal day 1–3 at experimental day 0) were used across different experimental days.

For microendoscopic or photometry recordings (Figs. 2, 3, 7, 8, and S1–S4), animals were placed in their home cage (191 × 376 × 163 mm) with standard wood chip bedding more than a day before the retrieval assay, which was conducted once a day for 3 consecutive days. The retrieval assay was carried out in the same manner as described above, with the assay duration extended to 6 min, the length of an imaging session. We waited more than 1 min before proceeding to the next imaging session in the case of Inscopix recordings. Following the retrieval assay on the first day, the tested virgin female was transferred to the cage of a mother and pups. For subsequent days, the cohoused mother and pups were temporally removed, and after connecting the animals to the imaging rigs, a 5–10-min wait was inserted before the imaging session. The same mother and pups were used for the assay and cohousing across different experimental days. The habituation process, involving connecting animals to the imaging rigs for 5–10 min, was conducted at least twice before the first imaging. An animal showing more than five retrievals per session for the first time was

defined as AP1 and the day following AP1 was defined as AP2. On the day for collecting Mother stage data, the pups were removed, leaving two to three pups in the nest. After a 2–3-min wait, an imaging session was initiated. For photometry recording with optogenetic silencing of the OFC (Figs. 5, 6, and S4), all the procedures were the same, but the duration per session was reduced to 2.5 min, and the interval between sessions was 2 min.

For microendoscopic recordings reported in Fig. 4, animals were placed in their home cage (191 × 376 × 163 mm) with standard wood chip bedding more than 1 day before the cohousing. After 2 or 3 days of cohousing, the habituation process and retrieval assay were carried out in the same manner as described above. The duration per session was 6 min, and two imaging sessions were conducted per animal.

In vivo microendoscopic imaging

For microendoscopic recording, a ProView GRIN lens (500-μm diameter, 4 mm length, Inscopix) insertion was performed (OFC, coordinates relative to the bregma: AP 2.5 mm, lateral 1.2 mm, depth 1.8 mm from the brain surface). Mice were anesthetized with 65 mg/kg ketamine (Daiichi-Sankyo) and 13 mg/kg xylazine (Sigma-Aldrich) via intraperitoneal injection and head-fixed to the stereotaxic equipment (Narishige). Next, we performed a craniotomy (1 mm diameter round shape) over the lens target area, clearing any remaining bone and overlying dura using fine forceps. We aspirated the brain tissue in 1 mm. Then, a GRIN lens was loaded onto the ProView lens holder and attached to Inscopix nVista. This unit was slowly lowered into the brain while we monitored the expression of GCaMP6s through nVista. Once the intended depth was reached and the signals from GCaMP6s were confirmed, we finalized the lens placement by permanently gluing the lens with Super-Bond (Sun Medical) and sealing the lens and skull together. In this step, we also glued a metal bar (Narishige, CF-10), which allowed us to attach and detach the microscope easily. After the glue was completely hardened, the camera and lens holder were carefully released from the lens, and Kwik-Kast (WPI) was used to protect the exposed lens surface. After more than 3 weeks of recovery, the mice were anesthetized and placed in the stereotaxic equipment again. The focal plane was adjusted until GCaMP6s-labeled cells were in focus, and then a baseplate (Inscopix) was permanently glued with Super-Bond. After more than a week of recovery, we attached the microscope and let the mice explore freely in their home cage for 5–10 min. We performed this habituation session more than twice before the first imaging session.

We performed microendoscopic imaging using the Inscopix nVista system (Inscopix). We performed imaging without refocusing the microscopes across imaging sessions during the day, whereas the focal plane was adjusted each day before the first imaging session. Before imaging, we attached the microendoscope to the animals while holding the implanted head bar. Images (1080 × 1080 pixels) were acquired using nVista HD software (Inscopix) at 10 Hz, with LED power of 0.4–1 mW/mm^2 and a gain of 2.0–3.0. Time stamps of the imaging frames, camera, delivery of sucrose water were collected for alignment using WaveSurfer (https://wavesurfer.janelia.org/). We performed

two imaging sessions, each lasting for 6 min, with an interval of a few minutes between sessions. The imaging data were cropped to 800 × 700 pixels and exported as .tiff files using the Inscopix Data Processing Software. To identify ROIs corresponding to putative cell bodies for the extraction of neural signals, we used v2 of MIN1PIPE (https://github.com/JinghaoLu/MIN1PIPE (*76*)) with a spatial down-sampling rate of 2. All traces from identified ROIs were manually inspected to ensure quality signals and excluded if they had an abnormal shape or overlapped signal from adjacent ROIs. Relative changes in calcium fluorescence F were calculated by $\Delta F/F_0 = (F-F_0)/F_0$ (where F_0 is the median fluorescence of the entire trace). $\Delta F/F$ was normalized within each cell. In the field of view, we typically detected 50.8 ± 11.1 (mean ± SD) ROIs.

To define significant responsive ROIs, trial-averaged Ca^{2+} signals were compared between the behavioral events and a baseline period using the Mann–Whitney U test, with a significance threshold of $p < 0.05$. Behavior videos were acquired at 20 Hz using a camera (Imaging source, DMK 33UX174). WaveSurfer was used to generate precise transistor-transistor logic (TTL) pulses to synchronize behavioral tracking and microendoscopic imaging. The animals that showed 10 or more successful pup retrievals were included in the following analysis. In Fig. 3, female mice among the AP1, AP2, and Mother stages showed a different number of retrieval trials. To normalize the statistical power across different stages, we randomly selected the same number of trials across each animal to determine responsive ROIs. The p-value was calculated by the mean of p-values based on 10,000 iterated calculations. Because the activity heat maps (Fig. 3B) showed no bimodal elevated or suppressed responses (e.g., elevated responses to both anticipatory and completion stages), we decided to classify cells into one of eight types, either elevated or suppressed in one of four behavioral categories. The following time windows were used for averaging: anticipatory, –1 to 0 s relative to the initiation of interaction; interaction, 0 to +1.5 s after the initiation of interaction; onset, 2 s following the onset of pup retrieval; and completion, 2 s following the completion of retrieval. The time window for the baseline was –1.5 to 0 s relative to each behavioral event. We first assigned elevated responding ROIs to anticipatory, interaction, onset of retrieval, or completion, in this order. In some cases, we noticed that the baseline fluctuated because of suppressed responses. For example, an ROI that showed a suppressed response to the interaction stage could be mistakenly assigned to an elevated responder to onset or completion because of the reduced baseline. In such cases, we retook the baseline –1.5 to 0 s relative to the initiation of interaction to recalculate the significance. Once all ROIs that showed elevated responses to one of four behavioral categories were assigned, we classified the remainder of the ROIs if they showed significant suppressed responses to anticipatory, interaction, onset of retrieval, or completion, in this order. To quantify response magnitude (Figs. 3, S1, and S3), we took a 3-s time window following each behavioral event to calculate the averaged response and subtracted this value from the mean of –2 to –0.5 s preceding the event as a baseline.

Decoder analysis

To decode a behavioral event between four different behavioral events (anticipatory vs. interaction vs.

onset vs. completion), we trained a set of binary SVM classifiers for multiclass classification using the one-vs.-one strategy through the MATLAB *fitcecoc* function (Fig. 3G–H). For training and testing of the SVM, we utilized data from the initial 10 retrieval trials, adjusting the number of trials to the minimum for fitting. In each run, the data were initially split into a training set and a test set at a 4:1 split ratio. The training process involved fivefold cross-validation to predict the detected behavior time series, with the calcium activity convolved over a 500-ms time window from the occurrence of each behavioral event. The outputs of the classifiers were combined, and the behavior with the highest number of votes was identified as the most likely behavior. Decoding accuracy was then estimated from the percentage of the test set correctly classified. Each classifier underwent 5,000 iterations, and the mean accuracy was subsequently calculated. Different combinations of ROIs were chosen randomly for each run.

To decode whether an interaction event was followed by retrieval or non-retrieval in Fig. 3I, we trained an SVM classifier using the MATLAB *fitcsvm* function. We used data from the first six retrievals and the first six non-retrieval trials to train and test the SVM. In each run, the data were initially divided into a training set and a test set at a 2:1 split ratio. The training was carried out using threefold cross-validation to predict the detected behavior time series, with the calcium activity convolved over a 500-ms time window from the timing of interaction with a pup. Decoding accuracy was then estimated from the percentage of the test set correctly classified. Each classifier underwent 10,000 iterations, and a mean accuracy was subsequently calculated. Different combinations of cells were chosen randomly for each run.

Nonsocial reward presentation

10% sucrose water was delivered from a behavioral lick port (Sanworks) controlled by an open-source code MATLAB-based state machine (Bpod; Sanworks). Mice could access the sucrose water whenever they broke an IR beam in front of the lick port and waited for longer than 1 s. To habituate the mice with the setup, we introduced this drinking port 1 day before the imaging session. After a habituation period of longer than 12 h, we deprived the water supply for 12–16 h to enhance the value of water. Then, we performed imaging with a pup retrieval assay. During the session, mice could freely access the licking port. For each animal, we performed two to four imaging sessions (duration 6 min). TTL pulses from the state machine were used to synchronize the timing of water delivery and microendoscopic imaging.

Test for significant overlap between nonsocial reward and pup-retrieval responses

To evaluate the significance of the overlap between ROIs responsive to water-reward-responsive and those responsive to pup-retrieval, a direct comparison was made between the observed fraction of ROIs responsive to both water reward and retrieval, and the fraction expected by chance. The chance overlap level was determined based on a null distribution created through the following procedure (*77*): cue-responsive and retrieval-responsive labels were randomly shuffled across all imaged ROIs

while maintaining the overall number of ROIs responsive to each event. Subsequently, the percentage of ROIs with these randomized labels being assigned as responsive to water reward and retrieval was noted. This random shuffling process was repeated 5,000 times, with each iteration recording the percentage of ROIs responsive to both water reward and pup retrieval. The significance of the observed overlap in our data was determined by comparing it with the simulated distribution.

Fiber photometry with optogenetic stimulation

For fiber photometry recording (Figs. 5, 6, and S4), *DAT-Cre/+; Ai162/+* double heterozygous female mice were used. We implanted the optical fibers (NA = 0.50, core diameter = 200 μm, 3 mm length from RWD) into the bilateral OFC for optogenetic stimulation at 2 weeks after AAV injection into the OFC (coordinates relative to the bregma: anterior 2.5 mm, lateral 0.6 mm, depth 1.7 mm from the brain surface with tilting 5° from the vertical). At the same surgery, an optical fiber (NA = 0.50, core diameter = 400 μm from Kyocera) was implanted above the VTA for fiber photometry. After surgery, the animals were crossed with stud males and housed in the home cage until recording. We performed Ca^{2+} imaging by delivering excitation lights (470 nm modulated at 530.481 Hz and 405 nm modulated at 208.616 Hz) and collected the emitted fluorescence using the integrated Fluorescence Mini Cube (Doric, iFMC4_AE(405)_E(460-490)_F(500-550)_S). Light collection, filtering, and demodulation were performed using the Doric photometry setup and Doric Neuroscience Studio Software (Doric Lenses, Inc.). The 405-nm signal was recorded as a background (non-calcium-dependent), and the 470-nm signal reported calcium-dependent GCaMP6s excitation/emission. The power output at the tip of the fiber was about 50 μW. The signals were initially acquired at 12 kHz and then decimated to 120 Hz. Next, we down-sampled the raw Ca^{2+} data to 20 Hz using the MATLAB *resample* function.

For optogenetic stimulation, animals were connected to a 465-nm laser (RWD) via split optical patch cords (NA = 0.50, core diameter = 200 μm, 200TH200FL1A; Thorlabs) and a rotary joint (RJ1; Thorlabs). For optogenetic inhibition of the OFC using GtACR2, 150 s of 465 nm continuous photostimulation at 5 mW/mm^2 at the fiber tip was used during the pup retrieval session. We first performed a photometry imaging session without light stimulation, followed by a session with light stimulation, which was repeated twice.

Fiber photometry with a $GRAB^{DA}$ sensor

For fiber photometry recording of DA dynamics (Figs. 7 and 8), a custom-built photometry system was used. The light from the fiber-coupled light-emitting diode (LED; 470 nm, M470F4, Thorlabs) was collimated (F950FC-A, Thorlabs) to pass through an excitation filter (MDF-GFP2 482-18, Thorlabs) and dichroic mirrors (MDF-GFP2, Thorlabs; ZT/405/488/561/647, Chroma). The filtered light was focused onto a fiber-optic patch cable (NA = 0.50, core diameter = 400 μm, MAF2L1, Thorlabs) through a rotary joint (RJ1; Thorlabs). The power output at the tip of the fiber was adjusted to 5 to 10 μW. The patch cable was connected to the optic fiber (NA = 0.50, core diameter =

400 μm, 6 mm length from RWD) implanted in the VS, DS, PS, or BLA. For isosbestic excitation at 405 nm, another light from the fiber-coupled LED (405 nm, M405FP1, Thorlabs) was collimated (F950FC-A, Thorlabs) and passed through an excitation filter (MF390-18, Thorlabs) and a dichroic mirror (MD416, Thorlabs) to merge with the 470 nm light path. The emission fluorescence was detected using a photomultiplier tube (PMT1001/M, Thorlabs) after passing through the dichroic mirror (ZT/405/488/561/647, Chroma) and an emission filter (MDF-GFP2 520-28, Thorlabs). LEDs were alternately illuminated for 4 ms with 6-ms intervals triggered by an open-source pulse generator (Pulse Pal v2, Sanworks) to detect signals at 470 nm and 405 nm separately. PMT signals were recorded at 1 kHz using a data acquisition system (PCIe-6341, National Instruments) and synchronized with a camera through WaveSurfer. The mean value of the middle 2-ms period during 4-ms LED illumination was used for analysis, which resulted in a 100 Hz signal. Signals were further decimated to 20 Hz after individual channel smoothing using the MATLAB *smooth* function with a LOWESS local linear regression method.

Photometry data analysis

We analyzed the photometry data using custom-written MATLAB codes. To calculate dF/F, a least-squares linear fit was applied to the 405-nm signal to align it to the 470-nm signal, producing a fitted 405-nm signal that was used to normalize the 470-nm signal using the MATLAB *polyfit* function. The ΔF/F was generated by subtracting the fitted 405-nm signal from the 470-nm signal to eliminate movement or other common artifacts. Finally, Ca^{2+} or DA traces were Z-scored by the mean and standard error of the traces for an entire recording session. To calculate the averaged response, we took a 2.5-s time window following the onset of the interaction, and that value was subtracted by the mean of –2 to –0.5 s preceding the interaction as a baseline.

To determine the specificity of DA transients in response to pup retrieval (Fig. 7E), we measured the AUC-ROC. This was calculated by comparing the distribution of calcium responses for each time frame along the trial (mean response for 10 frames, equivalent to 0.5 s from the time point) versus the distribution of calcium responses for the baseline (mean response from –3 to – 2 s before the interaction with a pup). The AUC-ROC value ranges from 0 to 1 and quantifies the accuracy of an ideal observer. Values proximal to 0.5 indicate low discrimination, whereas values far from 0.5 indicate high discrimination relative to baseline activity. To assess significance, we calculated the sample distribution by temporal shuffling within trials (n = 10 iterations). The timings where the signal exceeded the mean + 2SD of the sample distribution were defined as significant (Fig. 7E, red dots).

Pharmacogenetics

To activate (Fig. S2) or silence (Fig. 8) neural activity by hM3Dq or hM4Di, respectively, 100 μL of CNO (0.5 mg/mL, Sigma; C0832) was intraperitoneally injected after two 6-min imaging sessions (pre-CNO sessions). The two imaging sessions were performed 30 min after the injection of CNO

(post-CNO sessions).

Quantification and statistics

Statistical tests were performed using custom-written MATLAB codes. All tests were two-tailed. The sample size and statistical tests used are indicated in the figures or corresponding legends. The criterion for statistical significance was set at $P < 0.05$. The mean ± SEM was used to report statistics unless otherwise indicated. All of the tests that were used in this study and their p-values are summarized in the Supplementary Table (Table S1).

Data and materials availability

All data and custom-written MATLAB codes that support the findings of this study are available from the corresponding authors upon request.

References

1. C. Dulac, L. A. O'Connell, Z. Wu, Neural control of maternal and paternal behaviors. *Science* **345**, 765-770 (2014).
2. M. Numan, L. J. Young, Neural mechanisms of mother-infant bonding and pair bonding: Similarities, differences, and broader implications. *Horm Behav* **77**, 98-112 (2016).
3. L. Cohen, G. Rothschild, A. Mizrahi, Multisensory integration of natural odors and sounds in the auditory cortex. *Neuron* **72**, 357-369 (2011).
4. G. I. Tasaka, L. Feigin, I. Maor, M. Groysman, L. A. DeNardo, J. K. Schiavo, R. C. Froemke, L. Luo, A. Mizrahi, The Temporal Association Cortex Plays a Key Role in Auditory-Driven Maternal Plasticity. *Neuron* **107**, 566-579 e567 (2020).
5. A. Vinograd, Y. Fuchs-Shlomai, M. Stern, D. Mukherjee, Y. Gao, A. Citri, I. Davison, A. Mizrahi, Functional Plasticity of Odor Representations during Motherhood. *Cell Rep* **21**, 351-365 (2017).
6. G. I. Tasaka, C. J. Guenthner, A. Shalev, O. Gilday, L. Luo, A. Mizrahi, Genetic tagging of active neurons in auditory cortex reveals maternal plasticity of coding ultrasonic vocalizations. *Nat Commun* **9**, 871 (2018).
7. J. K. Schiavo, S. Valtcheva, C. J. Bair-Marshall, S. C. Song, K. A. Martin, R. C. Froemke, Innate and plastic mechanisms for maternal behaviour in auditory cortex. *Nature* **587**, 426-431 (2020).
8. B. J. Marlin, M. Mitre, A. D'Amour J, M. V. Chao, R. C. Froemke, Oxytocin enables maternal behaviour by balancing cortical inhibition. *Nature* **520**, 499-504 (2015).
9. M. Numan, D. S. Stolzenberg, Medial preoptic area interactions with dopamine neural systems in the control of the onset and maintenance of maternal behavior in rats. *Front Neuroendocrinol* **30**, 46-64 (2009).
10. J. Kohl, B. M. Babayan, N. D. Rubinstein, A. E. Autry, B. Marin-Rodriguez, V. Kapoor, K. Miyamishi, L. S. Zweifel, L. Luo, N. Uchida, C. Dulac, Functional circuit architecture underlying parental behaviour. *Nature* **556**, 326-331 (2018).
11. Y. Y. Fang, T. Yamaguchi, S. C. Song, N. X. Tritsch, D. Lin, A Hypothalamic Midbrain Pathway Essential for Driving Maternal Behaviors. *Neuron* **98**, 192-207 e110 (2018).
12. J. R. Moffitt, D. Bambah-Mukku, S. W. Eichhorn, E. Vaughn, K. Shekhar, J. D. Perez, N. D. Rubinstein, J. Hao, A. Regev, C. Dulac, X. Zhuang, Molecular, spatial, and functional single-cell profiling of the hypothalamic preoptic region. *Science* **362**, (2018).
13. C. Yoshihara, K. Tokita, T. Maruyama, M. Kaneko, Y. Tsuneoka, K. Fukumitsu, E. Miyazawa, K. Shinozuka, A. J. Huang, K. Nishimori, T. J. McHugh, M. Tanaka, S. Itohara, K. Touhara, K. Miyamichi, K. O. Kuroda, Calcitonin receptor signaling in the medial preoptic area enables risk-taking maternal care. *Cell Rep* **35**, 109204 (2021).

14. K. Miyamichi, Neural basis for behavioral plasticity during the parental life-stage transition in mice. *Front Neural Circuits* **17**, 1340497 (2023).
15. M. Febo, A. C. Felix-Ortiz, T. R. Johnson, Inactivation or inhibition of neuronal activity in the medial prefrontal cortex largely reduces pup retrieval and grouping in maternal rats. *Brain Res* **1325**, 77-88 (2010).
16. T. B. Franklin, B. A. Silva, Z. Perova, L. Marrone, M. E. Masferrer, Y. Zhan, A. Kaplan, L. Greetham, V. Verrechia, A. Halman, S. Pagella, A. L. Vyssotski, A. Illarionova, V. Grinevich, T. Branco, C. T. Gross, Prefrontal cortical control of a brainstem social behavior circuit. *Nat Neurosci* **20**, 260-270 (2017).
17. L. Kingsbury, S. Huang, J. Wang, K. Gu, P. Golshani, Y. E. Wu, W. Hong, Correlated Neural Activity and Encoding of Behavior across Brains of Socially Interacting Animals. *Cell* **178**, 429-446 e416 (2019).
18. M. Nakajima, A. Gorlich, N. Heintz, Oxytocin modulates female sociosexual behavior through a specific class of prefrontal cortical interneurons. *Cell* **159**, 295-305 (2014).
19. Z. Huang, M. Chung, K. Tao, A. Watarai, M. Y. Wang, H. Ito, T. Okuyama, Ventromedial prefrontal neurons represent self-states shaped by vicarious fear in male mice. *Nat Commun* **14**, 3458 (2023).
20. S. E. Silverstein, R. O'Sullivan, O. Bukalo, D. Pati, J. A. Schaffer, A. Limoges, L. Zsembik, T. Yoshida, J. J. O'Malley, R. F. Paletzki, A. G. Lieberman, M. Nonaka, K. Deisseroth, C. R. Gerfen, M. A. Penzo, T. L. Kash, A. Holmes, A distinct cortical code for socially learned threat. *Nature*, (2024).
21. C. E. Parsons, K. S. Young, M. V. Petersen, E. M. Jegindoe Elmholdt, P. Vuust, A. Stein, M. L. Kringelbach, Duration of motherhood has incremental effects on mothers' neural processing of infant vocal cues: a neuroimaging study of women. *Sci Rep* **7**, 1727 (2017).
22. M. Noriuchi, Y. Kikuchi, A. Senoo, The functional neuroanatomy of maternal love: mother's response to infant's attachment behaviors. *Biol Psychiatry* **63**, 415-423 (2008).
23. A. Izquierdo, Functional Heterogeneity within Rat Orbitofrontal Cortex in Reward Learning and Decision Making. *J Neurosci* **37**, 10529-10540 (2017).
24. A. Banerjee, G. Parente, J. Teutsch, C. Lewis, F. F. Voigt, F. Helmchen, Value-guided remapping of sensory cortex by lateral orbitofrontal cortex. *Nature* **585**, 245-250 (2020).
25. P. Y. Wang, C. Boboila, M. Chin, A. Higashi-Howard, P. Shamash, Z. Wu, N. P. Stein, L. F. Abbott, R. Axel, Transient and Persistent Representations of Odor Value in Prefrontal Cortex. *Neuron* **108**, 209-224 e206 (2020).
26. Y. Liu, Y. Xin, N. L. Xu, A cortical circuit mechanism for structural knowledge-based flexible sensorimotor decision-making. *Neuron* **109**, 2009-2024 e2006 (2021).

27. R. Basu, R. Gebauer, T. Herfurth, S. Kolb, Z. Golipour, T. Tchumatchenko, H. T. Ito, The orbitofrontal cortex maps future navigational goals. *Nature* **599**, 449-452 (2021).
28. J. Hirokawa, A. Vaughan, P. Masset, T. Ott, A. Kepecs, Frontal cortex neuron types categorically encode single decision variables. *Nature* **576**, 446-451 (2019).
29. J. H. Jennings, C. K. Kim, J. H. Marshel, M. Raffiee, L. Ye, S. Quirin, S. Pak, C. Ramakrishnan, K. Deisseroth, Interacting neural ensembles in orbitofrontal cortex for social and feeding behaviour. *Nature* **565**, 645-649 (2019).
30. B. J. Mattson, S. Williams, J. S. Rosenblatt, J. I. Morrell, Comparison of two positive reinforcing stimuli: pups and cocaine throughout the postpartum period. *Behav Neurosci* **115**, 683-694 (2001).
31. W. Schultz, P. Dayan, P. R. Montague, A neural substrate of prediction and reward. *Science* **275**, 1593-1599 (1997).
32. M. Watabe-Uchida, N. Uchida, Multiple Dopamine Systems: Weal and Woe of Dopamine. *Cold Spring Harb Symp Quant Biol* **83**, 83-95 (2018).
33. Y. Xie, L. Huang, A. Corona, A. H. Pagliaro, S. D. Shea, A dopaminergic reward prediction error signal shapes maternal behavior in mice. *Neuron* **111**, 557-570 e557 (2023).
34. M. Numan, D. S. Stolzenberg, A. A. Dellevigne, C. M. Correnti, M. J. Numan, Temporary inactivation of ventral tegmental area neurons with either muscimol or baclofen reversibly disrupts maternal behavior in rats through different underlying mechanisms. *Behav Neurosci* **123**, 740-751 (2009).
35. M. Watabe-Uchida, L. Zhu, S. K. Ogawa, A. Vamanrao, N. Uchida, Whole-brain mapping of direct inputs to midbrain dopamine neurons. *Neuron* **74**, 858-873 (2012).
36. K. T. Beier, E. E. Steinberg, K. E. DeLoach, S. Xie, K. Miyamichi, L. Schwarz, X. J. Gao, E. J. Kremer, R. C. Malenka, L. Luo, Circuit Architecture of VTA Dopamine Neurons Revealed by Systematic Input-Output Mapping. *Cell* **162**, 622-634 (2015).
37. V. M. K. Namboodiri, T. Hobbs, I. Trujillo-Pisanty, R. C. Simon, M. M. Gray, G. D. Stuber, Relative salience signaling within a thalamo-orbitofrontal circuit governs learning rate. *Curr Biol* **31**, 5176-5191 e5175 (2021).
38. T. R. Insel, L. J. Young, The neurobiology of attachment. *Nat Rev Neurosci* **2**, 129-136 (2001).
39. I. Carcea, N. L. Caraballo, B. J. Marlin, R. Ooyama, J. S. Riceberg, J. M. Mendoza Navarro, M. Opendak, V. E. Diaz, L. Schuster, M. I. Alvarado Torres, H. Lethin, D. Ramos, J. Minder, S. L. Mendoza, C. J. Bair-Marshall, G. H. Samadjopoulos, S. Hidema, A. Falkner, D. Lin, A. Mar, Y. Z. Wadghiri, K. Nishimori, T. Kikusui, K. Mogi, R. M. Sullivan, R. C. Froemke, Oxytocin neurons enable social transmission of maternal behaviour. *Nature*, (2021).
40. J. S. Rosenblatt, Nonhormonal basis of maternal behavior in the rat. *Science* **156**,

1512-1514 (1967).
41. C. H. Kinsley, M. Bardi, K. Karelina, B. Rima, L. Christon, J. Friedenberg, G. Griffin, Motherhood induces and maintains behavioral and neural plasticity across the lifespan in the rat. *Arch Sex Behav* **37**, 43-56 (2008).
42. J. H. Lui, N. D. Nguyen, S. M. Grutzner, S. Darmanis, D. Peixoto, M. J. Wagner, W. E. Allen, J. M. Kebschull, E. B. Richman, J. Ren, W. T. Newsome, S. R. Quake, L. Luo, Differential encoding in prefrontal cortex projection neuron classes across cognitive tasks. *Cell* **184**, 489-506 e426 (2021).
43. S. Gong, M. Doughty, C. R. Harbaugh, A. Cummins, M. E. Hatten, N. Heintz, C. R. Gerfen, Targeting Cre recombinase to specific neuron populations with bacterial artificial chromosome constructs. *J Neurosci* **27**, 9817-9823 (2007).
44. C. F. Yang, M. C. Chiang, D. C. Gray, M. Prabhakaran, M. Alvarado, S. A. Juntti, E. K. Unger, J. A. Wells, N. M. Shah, Sexually dimorphic neurons in the ventromedial hypothalamus govern mating in both sexes and aggression in males. *Cell* **153**, 896-909 (2013).
45. T. L. Daigle, L. Madisen, T. A. Hage, M. T. Valley, U. Knoblich, R. S. Larsen, M. M. Takeno, L. Huang, H. Gu, R. Larsen, M. Mills, A. Bosma-Moody, L. A. Siverts, M. Walker, L. T. Graybuck, Z. Yao, O. Fong, T. N. Nguyen, E. Garren, G. H. Lenz, M. Chavarha, J. Pendergraft, J. Harrington, K. E. Hirokawa, J. A. Harris, P. R. Nicovich, M. J. McGraw, D. R. Ollerenshaw, K. A. Smith, C. A. Baker, J. T. Ting, S. M. Sunkin, J. Lecoq, M. Z. Lin, E. S. Boyden, G. J. Murphy, N. M. da Costa, J. Waters, L. Li, B. Tasic, H. Zeng, A Suite of Transgenic Driver and Reporter Mouse Lines with Enhanced Brain-Cell-Type Targeting and Functionality. *Cell* **174**, 465-480 e422 (2018).
46. K. K. Ghosh, L. D. Burns, E. D. Cocker, A. Nimmerjahn, Y. Ziv, A. E. Gamal, M. J. Schnitzer, Miniaturized integration of a fluorescence microscope. *Nat Methods* **8**, 871-878 (2011).
47. K. Inada, M. Hagihara, K. Tsujimoto, T. Abe, A. Konno, H. Hirai, H. Kiyonari, K. Miyamichi, Plasticity of neural connections underlying oxytocin-mediated parental behaviors of male mice. *Neuron*, (2022).
48. C. M. Backman, N. Malik, Y. Zhang, L. Shan, A. Grinberg, B. J. Hoffer, H. Westphal, A. C. Tomac, Characterization of a mouse strain expressing Cre recombinase from the 3' untranslated region of the dopamine transporter locus. *Genesis* **44**, 383-390 (2006).
49. L. Yetnikoff, H. N. Lavezzi, R. A. Reichard, D. S. Zahm, An update on the connections of the ventral mesencephalic dopaminergic complex. *Neuroscience* **282**, 23-48 (2014).
50. Y. Zhuo, B. Luo, X. Yi, H. Dong, X. Miao, J. Wan, J. T. Williams, M. G. Campbell, R.

Cai, T. Qian, F. Li, S. J. Weber, L. Wang, B. Li, Y. Wei, G. Li, H. Wang, Y. Zheng, Y. Zhao, M. E. Wolf, Y. Zhu, M. Watabe-Uchida, Y. Li, Improved green and red GRAB sensors for monitoring dopaminergic activity in vivo. *Nature Methods*, (2023).

51. B. Dai, F. Sun, X. Tong, Y. Ding, A. Kuang, T. Osakada, Y. Li, D. Lin, Responses and functions of dopamine in nucleus accumbens core during social behaviors. *Cell Rep* **40**, 111246 (2022).
52. D. S. Stolzenberg, J. B. McKenna, S. Keough, R. Hancock, M. J. Numan, M. Numan, Dopamine D1 receptor stimulation of the nucleus accumbens or the medial preoptic area promotes the onset of maternal behavior in pregnancy-terminated rats. *Behav Neurosci* **121**, 907-919 (2007).
53. C. W. Henschen, R. D. Palmiter, M. Darvas, Restoration of dopamine signaling to the dorsal striatum is sufficient for aspects of active maternal behavior in female mice. *Endocrinology* **154**, 4316-4327 (2013).
54. D. Wei, V. Talwar, D. Lin, Neural circuits of social behaviors: Innate yet flexible. *Neuron* **109**, 1600-1620 (2021).
55. J. D. Wallis, Cross-species studies of orbitofrontal cortex and value-based decision-making. *Nat Neurosci* **15**, 13-19 (2011).
56. T. A. Stalnaker, N. K. Cooch, G. Schoenbaum, What the orbitofrontal cortex does not do. *Nat Neurosci* **18**, 620-627 (2015).
57. L. Kingsbury, S. Huang, T. Raam, L. S. Ye, D. Wei, R. K. Hu, L. Ye, W. Hong, Cortical Representations of Conspecific Sex Shape Social Behavior. *Neuron*, (2020).
58. T. Zhou, H. Zhu, Z. Fan, F. Wang, Y. Chen, H. Liang, Z. Yang, L. Zhang, L. Lin, Y. Zhan, Z. Wang, H. Hu, History of winning remodels thalamo-PFC circuit to reinforce social dominance. *Science* **357**, 162-168 (2017).
59. N. Padilla-Coreano, K. Batra, M. Patarino, Z. Chen, R. R. Rock, R. Zhang, S. B. Hausmann, J. C. Weddington, R. Patel, Y. E. Zhang, H.-S. Fang, S. Mishra, D. O. LeDuke, J. Revanna, H. Li, M. Borio, R. Pamintuan, A. Bal, L. R. Keyes, A. Libster, R. Wichmann, F. Mills, F. H. Taschbach, G. A. Matthews, J. P. Curley, I. R. Fiete, C. Lu, K. M. Tye, Cortical ensembles orchestrate social competition through hypothalamic outputs. *Nature* **603**, 667-671 (2022).
60. A. Corona, J. Choe, R. Munoz-Castaneda, P. Osten, S. D. Shea, A circuit from the locus coeruleus to the anterior cingulate cortex modulates offspring interactions in mice. *Cell Rep* **42**, 112771 (2023).
61. M. Nakajima, L. I. Schmitt, M. M. Halassa, Prefrontal Cortex Regulates Sensory Filtering through a Basal Ganglia-to-Thalamus Pathway. *Neuron* **103**, 445-458 e410 (2019).
62. L. A. Schwarz, K. Miyamichi, X. J. Gao, K. T. Beier, B. Weissbourd, K. E. DeLoach, J. Ren, S. Ibanes, R. C. Malenka, E. J. Kremer, L. Luo, Viral-genetic tracing of the

input-output organization of a central noradrenaline circuit. *Nature* **524**, 88-92 (2015).
63. W. Schultz, Behavioral theories and the neurophysiology of reward. *Annu Rev Psychol* **57**, 87-115 (2006).
64. W. Schultz, Dopamine reward prediction-error signalling: a two-component response. *Nat Rev Neurosci* **17**, 183-195 (2016).
65. L. Khouri, I. Nelken, Detecting the unexpected. *Curr Opin Neurobiol* **35**, 142-147 (2015).
66. H. Jeong, A. Taylor, J. R. Floeder, M. Lohmann, S. Mihalas, B. Wu, M. Zhou, D. A. Burke, V. M. K. Namboodiri, Mesolimbic dopamine release conveys causal associations. *Science* **378**, eabq6740 (2022).
67. Y. K. Takahashi, M. R. Roesch, R. C. Wilson, K. Toreson, P. O'Donnell, Y. Niv, G. Schoenbaum, Expectancy-related changes in firing of dopamine neurons depend on orbitofrontal cortex. *Nat Neurosci* **14**, 1590-1597 (2011).
68. J. F. Poulin, G. Caronia, C. Hofer, Q. Cui, B. Helm, C. Ramakrishnan, C. S. Chan, D. A. Dombeck, K. Deisseroth, R. Awatramani, Mapping projections of molecularly defined dopamine neuron subtypes using intersectional genetic approaches. *Nat Neurosci* **21**, 1260-1271 (2018).
69. A. Mohebi, J. R. Pettibone, A. A. Hamid, J. T. Wong, L. T. Vinson, T. Patriarchi, L. Tian, R. T. Kennedy, J. D. Berke, Dissociable dopamine dynamics for learning and motivation. *Nature* **570**, 65-70 (2019).
70. T. W. Bernklau, B. Righetti, L. S. Mehrke, S. N. Jacob, Striatal dopamine signals reflect perceived cue-action-outcome associations in mice. *Nat Neurosci*, (2024).
71. W. Menegas, K. Akiti, R. Amo, N. Uchida, M. Watabe-Uchida, Dopamine neurons projecting to the posterior striatum reinforce avoidance of threatening stimuli. *Nat Neurosci* **21**, 1421-1430 (2018).
72. A. C. Sias, Y. Jafar, C. M. Goodpaster, K. Ramirez-Armenta, T. M. Wrenn, N. K. Griffin, K. Patel, A. C. Lamparelli, M. J. Sharpe, K. M. Wassum, Dopamine projections to the basolateral amygdala drive the encoding of identity-specific reward memories. *Nat Neurosci*, (2024).
73. M. Mahn, L. Gibor, P. Patil, K. C.-K. Malina, S. Oring, Y. Printz, R. Levy, I. Lampl, O. Yizhar, High-efficiency optogenetic silencing with soma-targeted anion-conducting channelrhodopsins. *Nat Commun* **9**, 4125 (2018).
74. E. S. Lein, M. J. Hawrylycz, N. Ao, M. Ayres, A. Bensinger, A. Bernard, A. F. Boe, M. S. Boguski, K. S. Brockway, E. J. Byrnes, L. Chen, L. Chen, T. M. Chen, M. C. Chin, J. Chong, B. E. Crook, A. Czaplinska, C. N. Dang, S. Datta, N. R. Dee, A. L. Desaki, T. Desta, E. Diep, T. A. Dolbeare, M. J. Donelan, H. W. Dong, J. G. Dougherty, B. J. Duncan, A. J. Ebbert, G. Eichele, L. K. Estin, C. Faber, B. A. Facer, R. Fields, S. R. Fischer, T. P. Fliss, C. Frensley, S. N. Gates, K. J. Glattfelder, K. R. Halverson, M. R.

Hart, J. G. Hohmann, M. P. Howell, D. P. Jeung, R. A. Johnson, P. T. Karr, R. Kawal, J. M. Kidney, R. H. Knapik, C. L. Kuan, J. H. Lake, A. R. Laramee, K. D. Larsen, C. Lau, T. A. Lemon, A. J. Liang, Y. Liu, L. T. Luong, J. Michaels, J. J. Morgan, R. J. Morgan, M. T. Mortrud, N. F. Mosqueda, L. L. Ng, R. Ng, G. J. Orta, C. C. Overly, T. H. Pak, S. E. Parry, S. D. Pathak, O. C. Pearson, R. B. Puchalski, Z. L. Riley, H. R. Rockett, S. A. Rowland, J. J. Royall, M. J. Ruiz, N. R. Sarno, K. Schaffnit, N. V. Shapovalova, T. Sivisay, C. R. Slaughterbeck, S. C. Smith, K. A. Smith, B. I. Smith, A. J. Sodt, N. N. Stewart, K. R. Stumpf, S. M. Sunkin, M. Sutram, A. Tam, C. D. Teemer, C. Thaller, C. L. Thompson, L. R. Varnam, A. Visel, R. M. Whitlock, P. E. Wohnoutka, C. K. Wolkey, V. Y. Wong, M. Wood, M. B. Yaylaoglu, R. C. Young, B. L. Youngstrom, X. F. Yuan, B. Zhang, T. A. Zwingman, A. R. Jones, Genome-wide atlas of gene expression in the adult mouse brain. *Nature* **445**, 168-176 (2007).

75. K. K. Ishii, T. Osakada, H. Mori, N. Miyasaka, Y. Yoshihara, K. Miyamichi, K. Touhara, A Labeled-Line Neural Circuit for Pheromone-Mediated Sexual Behaviors in Mice. *Neuron* **95**, 123-137 e128 (2017).

76. J. Lu, C. Li, J. Singh-Alvarado, Z. C. Zhou, F. Frohlich, R. Mooney, F. Wang, MIN1PIPE: A Miniscope 1-Photon-Based Calcium Imaging Signal Extraction Pipeline. *Cell Rep* **23**, 3673-3684 (2018).

77. L. Willmore, A. R. Minerva, B. Engelhard, M. Murugan, B. McMannon, N. Oak, S. Y. Thiberge, C. J. Pena, I. B. Witten, Overlapping representations of food and social stimuli in mouse VTA dopamine neurons. *Neuron* **111**, 3541-3553 e3548 (2023).